



Assessing the hazard of fault triggering by deep geothermal energy production in an active fault system via a 1D stress model and 3D fault mapping

Nicola Levi¹ · Michael Weissl¹ · Kurt Decker¹

Received: 30 March 2023 / Accepted: 27 December 2023 / Published online: 27 March 2024
© The Author(s) 2024

Abstract

Borehole image data and a 1D-stress model built on open hole logs, leak-off tests (LOT) and image logs are used to evaluate the potential of seismicity caused by fault triggering during geothermal heat production in the city of Vienna. Data were derived from a 4220 m deep geothermal exploration well that investigated the geothermal potential of fractured carbonates below the Miocene fill of the Vienna Basin. The well penetrated several normal faults of the Aderklaa Fault System (AFS) that offset Pleistocene terraces at the surface and hence are regarded as active. Stress-induced borehole failures and 1D geomechanical modeling proves that the potential reservoirs are in a normal fault stress regime with $S_v > S_{Hmax} > S_{Hmin}$. While stress magnitudes in the upper part of the well (down to about 2000 m) are significantly below the magnitudes that would trigger the rupture of critically oriented faults including the AFS, stresses in the lower part of the drilled section in the pre-Neogene basement (below about 3300 m) are not. Data evidence a rotation of S_{Hmax} for about 45° at a fault of the AFS at 3694 m to fault-parallel below the fault suggesting that the fault is active. Critical or near-critical stressing of the fault is corroborated by the stress magnitudes calculated from the 1D geomechanical model. The safety case to exclude unintended triggering of seismic fault slip by developing geothermal reservoirs in close vicinity to one of the branch faults of the AFS may therefore be difficult or impossible to make.

Keywords Triggered seismicity · Geothermal exploration · Active faulting · Vienna basin

Introduction

In the last decades, the increasing need for renewable energies led to an exponential growth of enhanced geothermal projects in many parts of the World, including continental Europe, that led to several episodes of unpredicted induced seismicity (Majer et al. 2007; Witze 2017; Buijze et al. 2020), which in some instances brought to the temporary interruption of the geothermal activities or even to the complete cancelation of projects (SERIANEX 2009; Diehl et al. 2017). In particular, after the unsuccessful geothermal project in Basel (Switzerland), which experienced seismicity up

to M 3.4, the enhanced geothermal projects are facing criticism. Unwanted seismicity can occur during the stimulation phase (Baisch et al. 2006; Häring et al. 2008; Deichmann and Ernst 2009) or normal production activities (Kwiattek et al. 2015), as in both cases fluids are injected into the subsurface, resulting in pore pressure build-up associated with the decrease of the effective normal stress acting on faults, which could lead to unpredicted fault-slip and triggered seismicity (Catalli et al. 2013; Kim 2013). In the case of triggered seismicity, human intervention causes the initiation of the seismic rupture process of a fault while the subsequent rupture propagation is controlled by natural stress. Triggered earthquakes are advanced by human intervention and natural stress aggravates the ground shaking.

A reliable physical upper bound of the maximum credible triggered earthquake may only be estimated from the size of the triggered fault using established scaling laws (e.g., Wells and Coppersmith 1994). Fault triggering was reported to result in earthquakes with comparably large magnitudes such as the $M_w = 5.5$ ($I_0 =$ VIII MMI) 2017 Pohang earthquake

✉ Kurt Decker
kurt.decker@univie.ac.at

Nicola Levi
nicola.levi@univie.ac.at

¹ Department of Geology, University of Vienna, Althanstraße 14, 1090 Vienna, Austria

(Grigoli et al. 2018; Choi et al. 2019; Woo et al. 2019). Such events cannot be tolerated as side effects of geothermal heat production in populated areas. The planning and implementation of a geothermal project, therefore, requires a safety case which accounts for the actual tectonic situation and natural stress in the project area to exclude unintended triggering of seismic fault slip. This may be achieved by demonstrating that (1) faults with significant sizes are sufficiently remote and will not be affected by human-induced stress changes, (2) faults are oriented unfavorably with respect to the current stress field thus prevent triggering, and/or (3) human-induced stress changes will not suffice to reach a critical state of stress.

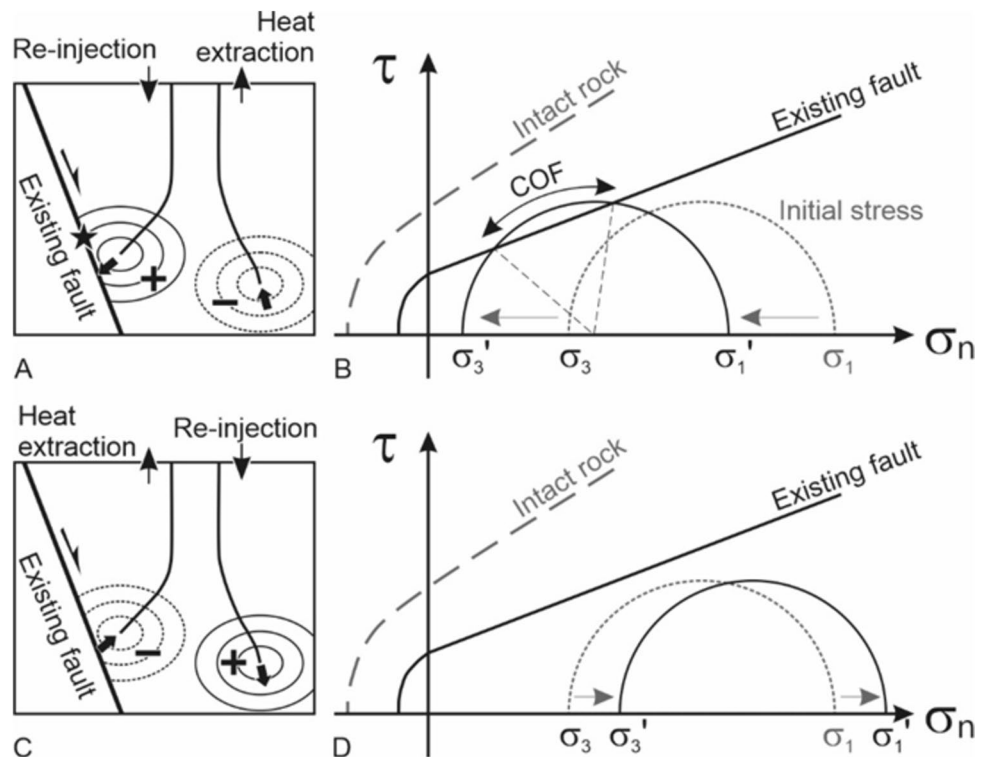
Figure 1 shows a scenario where geothermal heat extraction and the re-injection of cooled water leads to pore pressure increase in the vicinity of a pre-existing fault (Fig. 1a) and a schematic representation of the resulting stress change near to the fault, due to lowering the magnitude of the effective stresses (stress magnitude minus the corresponding pore pressure), that eventually leads to critical stressing of part of the fault and its triggering (Fig. 1b). It is evident that fault slip is aided by initial stress represented by a Mohr circle close to the failure envelope and by a favorable orientation of the fault. In this case a safety demonstration needs to demonstrate that pressure buildup will not result in critical stress states for critically oriented faults. This demonstration requires well-constrained stress data, kinematic fault data (orientation and failure envelope), and robust estimates of the increase of pore pressure, the later depending on parameters such as injection rate, reservoir permeability,

and temperature changes. An alternative scenario, achieved by swapping the production and injection wells, is shown in Fig. 1c, d. In deep geothermal fields, the thermo-elastic stresses resulting from the injection of colder fluids into the reservoir might further destabilize the stress system, in particular, in the case of high enthalpy system (Evans et al. 2012; Martínez-Garzón et al. 2016; Buijze et al. 2020).

Exploration of the deep geothermal potential for the city of Vienna is still in an early stage. However, almost from its beginning, exploration included assessments of the potential of triggered and induced seismicity. This is due to the fact that, first, the threshold of tolerable earthquakes in the urban environment of Vienna is very low and, second, exploration focuses on an area with numerous active and potentially active faults belonging to the Vienna Basin Transfer Fault System. The activity of the fault system is evident from seismological, paleoseismological, and geological data (Gutdeutsch and Aric 1988; Decker et al. 2005; Hinsch et al. 2005; Apoloner et al. 2015; Hintersberger et al. 2018; Weissl et al. 2017). It has to be assumed that these active and potentially active faults are close to critical stressing.

In 2012, a geothermal exploration well was drilled within the city limits of Vienna (Well 1; Figs. 2, 3), in which open hole logs, image logs, and geomechanical data (leak-off tests) were acquired. More recently, in a new era of geothermal exploration, 2D and 3D reflection seismic were acquired in the urban area of Vienna. We use these data to constrain the current stress field in the exploration area and estimate the distance to failure for a

Fig. 1 Schematic diagrams illustrating the effects of pore pressure changes due to geothermal heat production. **A** Scheme of a doublet with re-injection in the vicinity of pre-existing fault. **B** Mohr diagram and Griffith-Coulomb failure envelope illustrating the shift of the Mohr circle towards the failure envelope by reducing effective stress (stress-pore pressure). **C** Doublet extracting fluid from a volume close to a fault **D** leading to a right-shift of the Mohr circle by increasing effective stress. σ_1, σ_3 : initial stress; σ_1', σ_3' : effective stress; COF: segment of the Mohr circle representing critically oriented faults



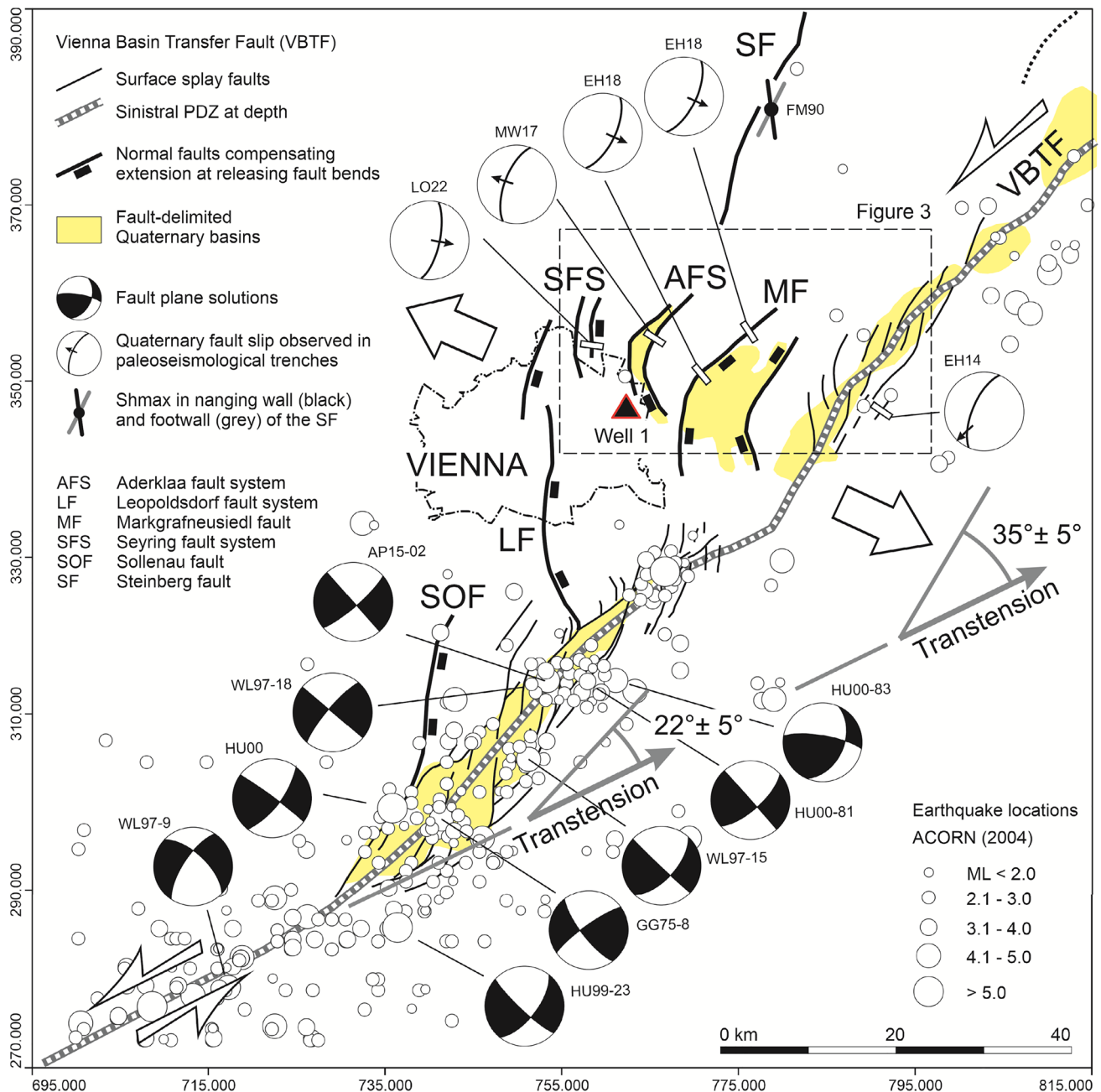


Fig. 2 Tectonic sketch map summarizing evidence of active faulting in the Vienna Basin (synthesized from Decker et al. 2005; Beidinger and Decker 2011). Note the releasing bends of the VBTF and locations of normal faults compensating transtension at these bends. References: AP15: Apoloner et al. (2015); EH14: Hintersberger et al.

2014; EH18: Hintersberger et al. (2018); FM90: Marsch et al. (1990); GG75: Gangl (1975); HU99, HU00: Tóth et al. (1999), 2000; WL97: Lenhardt 1997, pers. comm; see also Reinecker and Lenhardt (1999); MW17: Weissl et al. (2017); LO: Oppenauer et al. (2022). Seismic events are derived from the database ACORN (2004)

group of sub-parallel active normal faults locally referred to the Aderklaa Fault System (AFS).

Geologic background

Geothermal exploration focuses on deep aquifers in the Vienna Basin, a pull-apart basin that formed in the Miocene (Royden 1985; Wessely 1988; Decker 1996). Pull-apart basins are tectonic depressions dominated by systems

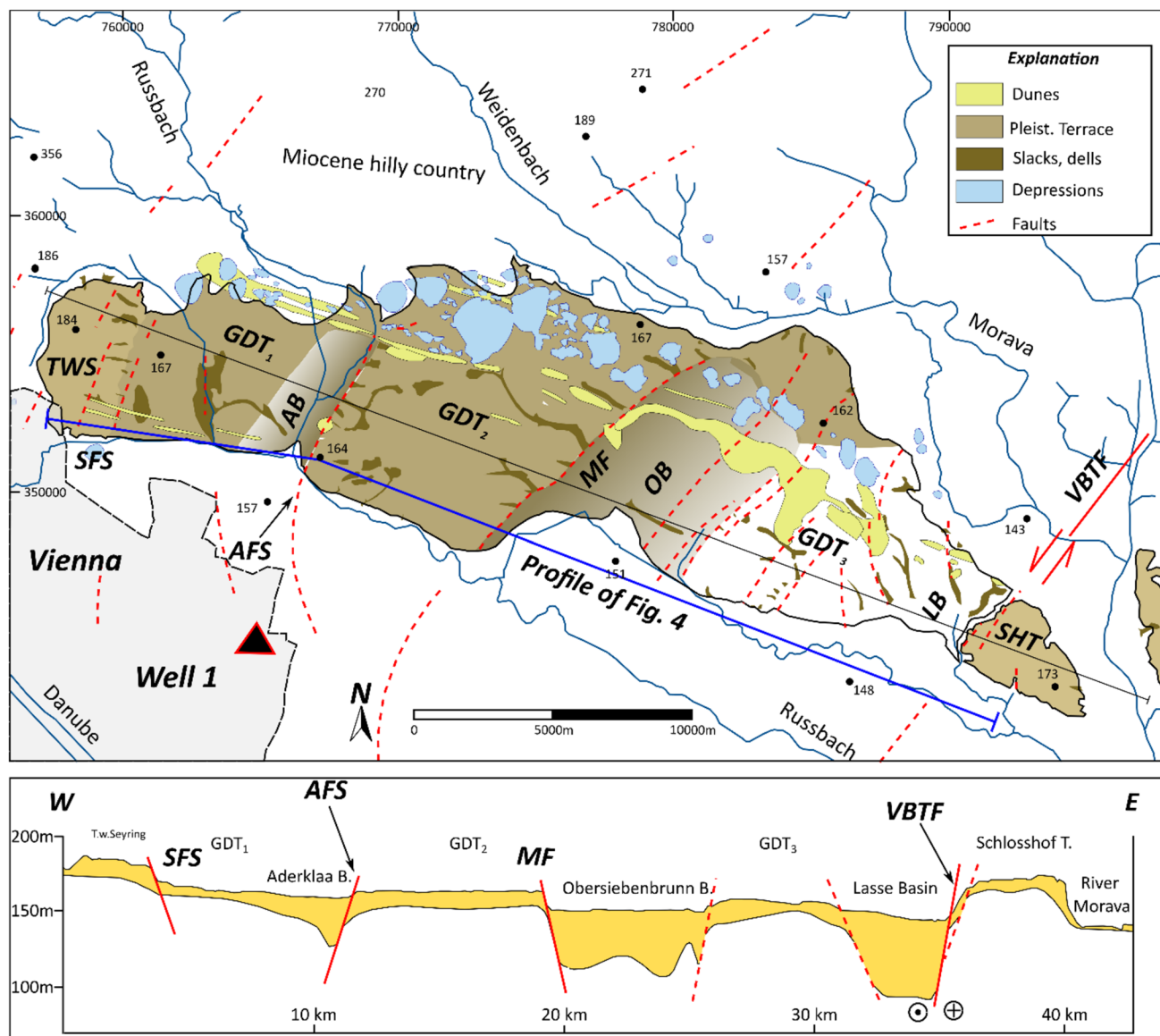


Fig. 3 **A** Geomorphological map of the Marchfeld area of the Vienna Basin showing the locations of Quaternary faults offsetting the Pleistocene Gänsersdorf Terrace (modified from Weissl et al. 2017). **B** Cross-section denoting the locations of fault scarps delimiting the Gänsersdorf Terrace and fault-delimited Quaternary basins. AB:

Aderklaa Basin; AFS: Aderklaa Fault System; GDT: Gänsersdorf Terrace; LB: Lasse Basin; MF: Markgrafneusiedl Fault; OB: Obersiebenbrunn Basin; SHT: Schlosshof Terrace; TWS: Terrace West of Seyring; VBTF: Vienna Basin Transfer Fault System. The blue line indicates the position of profile in Fig. 4

of normal faults, which are formed in the area comprised between two stepped strike-slip faults with same kinematics, usually with similar orientation (Aydin and Nur 1982). Explored aquifers are located both, within the Miocene fill of the pull-apart basin and in the pre-Miocene basement. The latter is represented by the dismembered fold-thrust nappes of the external Eastern Alps with Rheno-Danubian Flysch and the Northern Calcareous Alps (Kröll and Wessely 1993). These units are overlain by the Early Miocene sediments of a wedge-top basin system that was deposited on the frontal part of the Eastern Alpine allochthon during the final stages

of fold-thrusting (Hölzel et al. 2010). Pull-apart subsidence commenced in the Midde Miocene at the left-stepping sinistral Vienna Basin Transfer Fault System (VBTF; Royden 1985; Fig. 2). The associated basin fill consists of several shallow-marine, limnic and fluvial sedimentary sequences mostly represented by shales, sandstones and marls deposited between the Lower Badenian and the Upper Pannonian (Arzmüller et al. 2006; Strauss et al. 2006; Lee and Wagreich 2017; Harzhauser et al. 2020). These sediments reach a maximum thickness of close to 5000 m in the basin depocenters. The maximum strike-slip activity was located close

to the SE basin boundary, where a principle displacement zone (PDZ) with prominent negative flower structures formed. These flower structures form up to 10 km wide systems of en-echelon faults at surface. The largest normal faults are aligned with the NW basin margin resulting in a rather asymmetric basin shape (Sollenau, Leopoldsdorf and Steinberg fault; Kröll and Wessely 1993; Lee and Wagreich 2017; Fig. 2). The normal faults branch from releasing bends of the strike-slip system. Pull-apart subsidence terminated in the Upper Pannonian due to regional stress change leading to localized inversion of the Vienna Basin structures (Decker and Peresson 1996; Peresson and Decker 1997).

Quaternary to recent tectonics of the Vienna Basin is characterized by the sinistral re-activation of the VBTF as evidenced by the distribution of seismicity along the strike-slip fault, fault plane solutions, and the subsidence of Quaternary pull-apart basins on top of negative flower structures along the VBTF (Gutdeutsch and Aric 1988; Decker et al. 2005; Hinsch et al. 2005; Lenhardt et al. 2007; Beidinger et al. 2011; Hammerl and Lenhardt 2013; Nasir et al. 2020; Fig. 2). Almost all of the seismic activity is observed along the VBTF at the SE boundary of the basin, whereas historical and instrumental seismicity is very low in the basin center and on the normal fault systems that splay from the main strike-slip faults. Unequivocal evidence of the activity of normal faults in the Vienna Basin, however, comes from

geomorphological, Quaternary and paleoseismological data. Hinsch et al. (2005) have shown that Pleistocene river terraces of the Danube are tilted by hanging wall rollover above the Leopoldsdorf fault. Decker et al. (2005) and Weissl et al. (2017) provided evidence of the displacement of river terraces, Quaternary growth faulting and basin formation at the Seyring (SFS) and Aderklaa fault system (AFS) as well as the Markgrafneusiedl fault (Fig. 3). Paleoseismological data from the AFS (Weissl et al. 2017), the Markgrafneusiedl fault (Hintersberger et al. 2018) and the SFS (Oppenauer et al. 2022) demonstrate that these normal faults have been the locations of strong paleo-earthquakes with magnitudes estimated from surface displacements ranging between 6.2 ± 0.5 and 6.8 ± 0.4 for the Markgrafneusiedl fault, and about $M = 6.4$ for the SFS.

Active faulting of the Steinberg fault is corroborated by a switch of the orientation of S_{Hmax} from about N–S in the hangingwall to SSW–NNE (i.e., parallel to fault strike) in the footwall of the normal fault (Marsch et al. 1990) with the fault-parallel S_{Hmax} possibly indicating a normal faulting stress regime. Beidinger and Decker (2011) related the activity of the normal splay faults of the VBTF strike-slip system to two prominent releasing bends in the southern and central Vienna Basin where fault strike changes for about 22° and 35° , respectively, causing transtension and extension

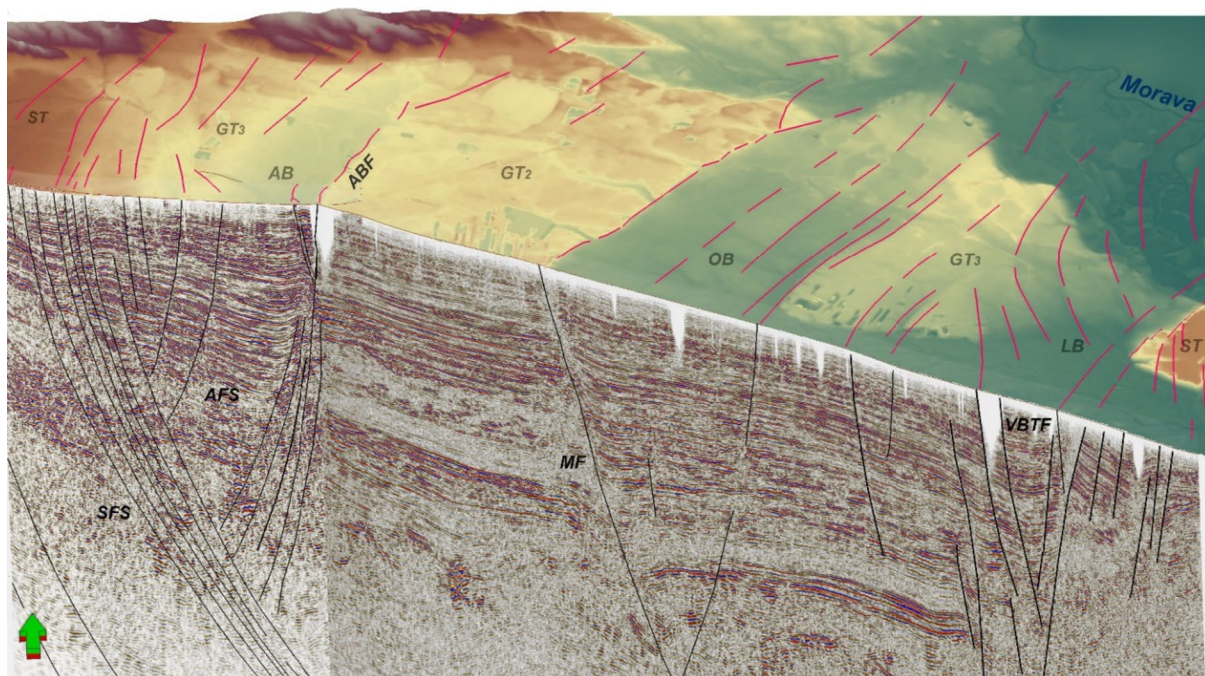


Fig. 4 Regional 2D seismic cross section through the central Vienna Basin showing the main normal fault systems (SFS: Seyring fault system; AFS: Aderklaa fault system; MF: Markgrafneusiedl fault) and the negative flower structure of the Vienna Basin Transfer Fault System (VBTF) together with tectonic geomorphology of Pleisto-

cene river terraces (ST: Seyring terrace; GT: Gänserndorf terrace; ST: Schlosshof terrace) and Quaternary basins that formed on top of the faults (AB: Aderklaa basin; OB: Obersiebenbrunn basin; LB: Lasse basin)

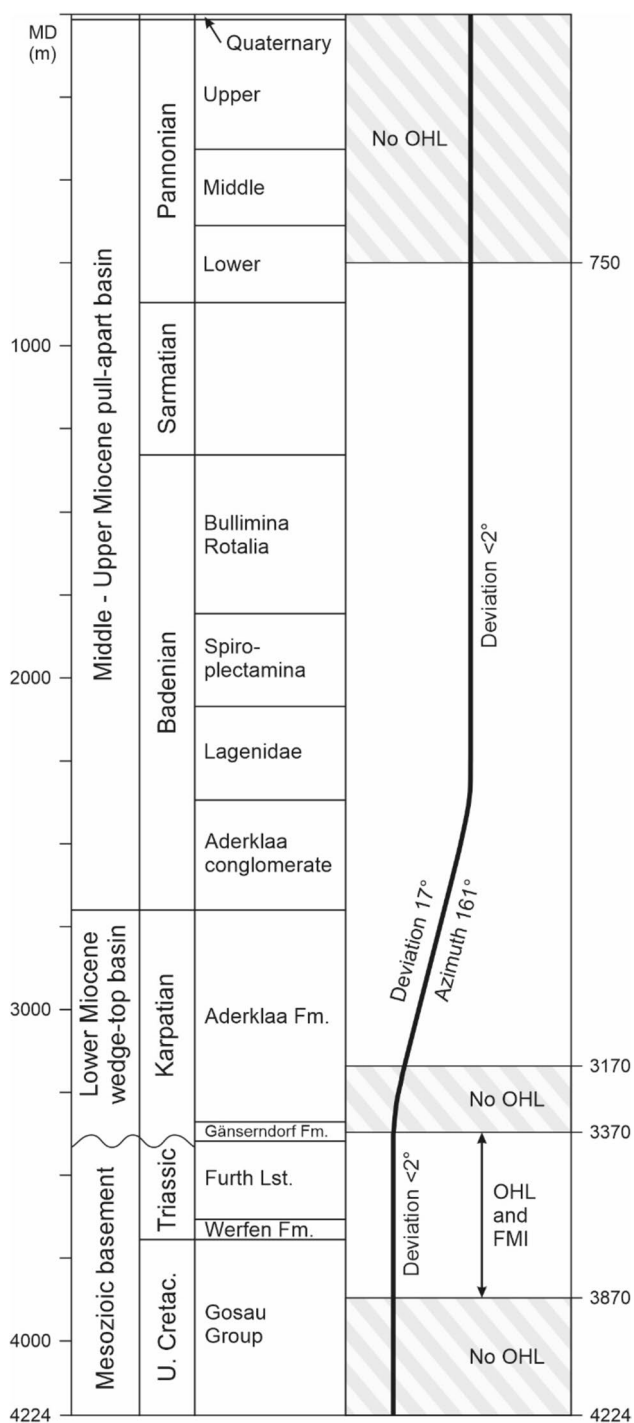


Fig. 5 Well stratigraphy, data coverage and inclination of the geothermal exploration Well 1. MD: Measured Depth. OHL: open hole logs

perpendicular to VBTF in the part of the basin NW of the releasing knickpoints (Fig. 2).

Exploration of the deep geothermal potential for the city of Vienna and Well 1 focused on reservoirs below the Miocene fill of the Vienna Basin in the area close to and between the SFS and AFS (Fig. 4). A geomorphological map of the

area shows that both fault systems form fault scarps offsetting the Pleistocene Gänserndorf Terrace, deviate the fluvial system of the Russbach (Fuchs and Grill 1984; Weissl et al. 2017), and cause the subsidence of the up to 30 m deep Quaternary Aderklaa basin (Fig. 3b). Faulted Quaternary sediments have been observed along the boundaries of the GDT₂ terrace, suggesting recent tectonic activity (Posch-Trötzmüller and Peresson 2010; Weissl et al. 2017). For the AFS, a slip rate of 0.05 mm/y was estimated based on the ages of offset terrace sediments (200–300 ka) and post-Pleistocene covers (15 ka) (Weissl et al. 2017). Regional seismic cross sections show that the SFS comprises of a series of E-dipping normal faults that are located next to the W border of the pull-apart basin (Fig. 4). The WNW- to WSEW-dipping normal faults of the AFS are interpreted to abut against the SFS at depth. The exploration Well 1, located about 5 km S of the regional cross section shown in Fig. 4, drilled several branch faults of the AFS.

Well data

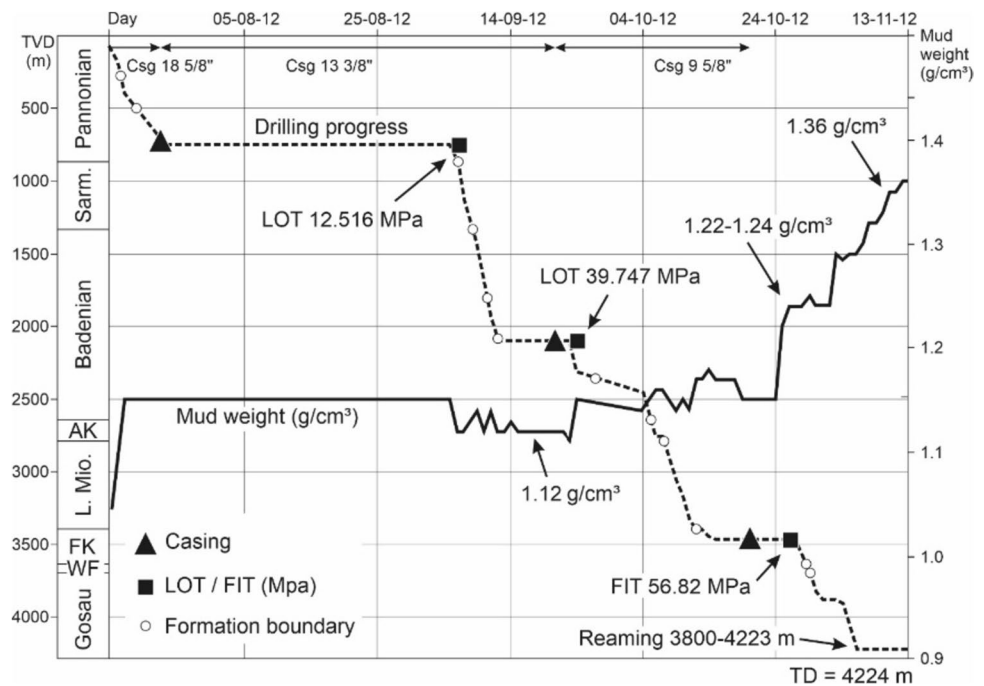
Well 1 is located within the urban area of Vienna, South of the Gänserndorf Terrace, in the Danube lowlands where the AFS is buried below Holocene fluvial gravels and overbank fines of the Danube (Fig. 3A). The 4224 m deep well was drilled with a nearly vertical trajectory, with just the central section deviated up to 17° towards 161° (2200–3499 m MD) (Fig. 5). From top to base, the Miocene section of the borehole (11–3397 m MD) consists of shales, marls, and sandstones of the Pannonian stage, Sarmatian marl with minor sandstones, and middle-upper Badenian marl. The lower Badenian consists of the Aderklaa Fm., subdivided into an upper conglomerate forming a prominent aquifer, and a lower sandy section. In Well 1, the base of the Miocene basin fill is represented by the Gänserndorf Conglomerate (Fig. 5). The pre-Neogene basement of the Vienna Basin consists of successions belonging to the Northern Calcareous Alps, with lower-middle Anisian shallow-marine limestones (Furth Lst.; Moser and Piros 2018), lower Triassic siliciclastic Werfen Fm. and anhydrite (3633–3694 m). The lowermost part of the borehole drilled Upper Cretaceous sandy marls of the Gosau Group (Fig. 5).

Several runs of open hole logs (OHL) are available from Well 1, including various curves and covering different depth intervals (Table 1). Two data gaps with no OHL occur between about 3170 and 3373 m MD and below 3884 m. Curves measuring the borehole diameter from not oriented caliper are available covering various sections of Well 1. Two types of not oriented caliper curves are available in the well: the curve labeled BD (interval 750–2090 m) is an individual measurement of the borehole diameter on two

Table 1 Available logs in Well 1, with the corresponding depth intervals in measured depth (MD)

Gamma Ray GR (m)	Density RHOZ (m)	Sonic DTCO (m)	Phot. Fact PE (m)	Resistivity RL	Neut. Por NPHI (m)	Not oriented caliper		Image Log FMI (m)
						2-arm (BD curves) (In)	6-arm (HD curves) (In)	
0–3370	756–3170	740–3170	751–3161	1748–3170	0–2075	740–2082		
							2099–3178	
3370–3877	3370–3876	3370–3855	3370–3860	3370–3868				3373–3884

Fig. 6 Summary of the drilling experience in Well 1, based on data of the daily mud reports. Csg: casing; FIT: formation integrity test; LOT: leak-off test; AK: Aderklaa conglomerate; FK: Furth Lst.; WF: Werfen Fm. TVD is True Vertical Depth



opposite arms; curves HD (HD-1, HD-2, HD-3; interval 2099–3178 m) derive from 6 arm caliper and display the borehole diameter between two opposite arms (Table 1). One single image log (FMI) was acquired in the lower part of the well (3373–3884 m) (Fig. 5; Table 1).

Daily mud density data are recorded in drilling reports. The well was initially drilled with a mud density in the range 1.12–1.17 g/cm³ without any significant issues (Fig. 6). Between 3473 and 3880 m, a mud weight of 1.22–1.24 g/cm³ was initially used. Below 3880 m, the mud density was subsequently raised to 1.29 g/cm³ and finally to 1.36 g/cm³ (Fig. 6). Repeated reaming was attempted in the interval 3800–4223 m to keep the borehole on gauge. The results of two leak-off tests (LOT) were acquired at 754 m MD (754 m TVD) (upper Pannonian silty shales) and 2103 m MD (2103 m TVD) (Badenian siltstones), providing a fracture pressures of respectively 12.516 MPa and 39.747 MPa. No raw LOT were provided, but just the results of the tests as fracture gradients that have been converted into absolute pressures using the corresponding TVD. Thus, these data are

not replicable and should be classified as D quality in the quality ranking for stress measurements proposed by Morawietz et al. (2020). A third test at 3437.6 m MD (3399.9 m TVD) (in Triassic limestones) did not reach the breaking point and is labeled as formation integrity test (FIT) (56.82 MPa).

Structural analysis of the FMI data

Stress-induced failures are the result of the stress perturbations generated along the borehole wall, when stressed rocks are replaced with drilling fluid (Fig. 7). The stresses acting on the borehole wall can be subdivided into three components: the axial stress acting along the borehole axis, the radial stress, and the hoop stress acting along the circumference of the borehole wall. Both the axial stress and hoop stress change greatly in magnitude with azimuth, whereas the radial stress is constant (Fig. 7a; Moos and Zoback 1990; Zoback 2007). As a result, the stress perturbation around the well leads to the development of

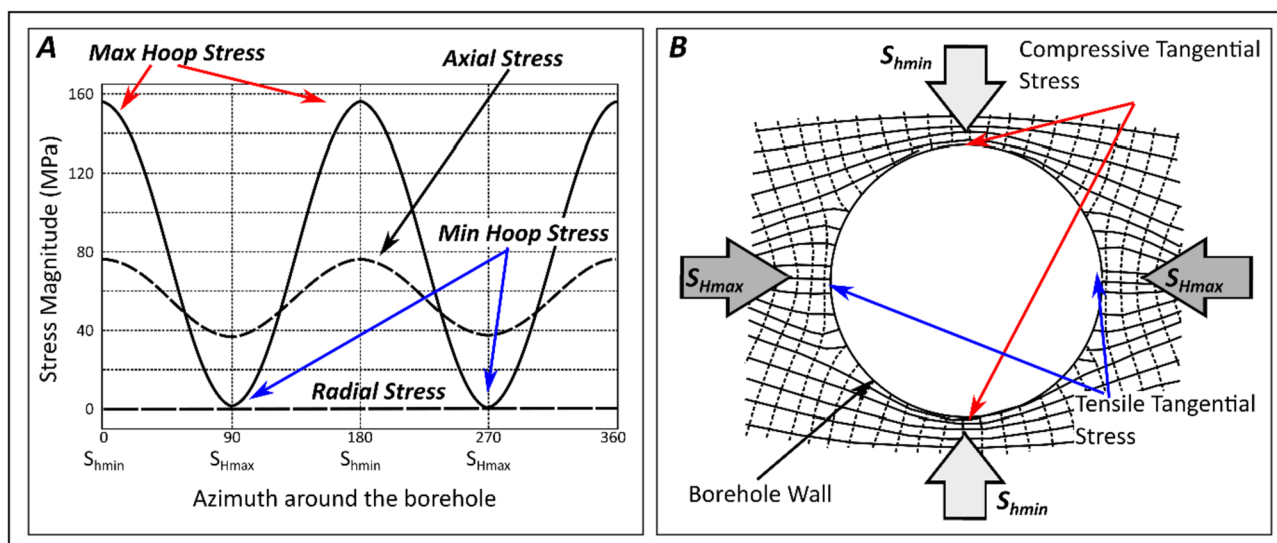


Fig. 7 **A** Diagram showing the variation of the stress magnitudes along the wall of a vertical borehole. In this example, S_{Hmax} is oriented E-W. The hoop stress reaches maximum and minimum magnitudes at the azimuth of the S_{hmin} and S_{Hmax} (after Zoback 2007). **B**

Sketch of the stress perturbation surrounding a vertical borehole showing the relationships between horizontal stresses S_{Hmax} and S_{hmin} , and the azimuth of the borehole sectors with compressive and tensile tangential stresses (modified after Kirsch 1898)

symmetric compressive and extensional tangential stresses along the borehole wall (Fig. 7b). The complex relationship between the various components of the geomechanical model defines the conditions that might lead the borehole to fail into tension (in the sectors with tensile tangential stresses) or into compression (in the area with compressive tangential stresses) (Zoback et al. 1985, 2003; Bell 1990; Moos and Zoback 1990; Zoback 2007; Heidbach et al. 2016).

Borehole Breakout (BO) is typically observed in the borehole sectors with compressive tangential stresses and consists of two symmetric areas where the borehole was enlarged (Heidbach et al. 2016). Drilling-induced tensile fractures (DITF) can develop in the borehole sectors with tensile tangential stress, appearing as two symmetric open fractures elongated parallel to the borehole axis. In vertical wells, the azimuth of BO is parallel to the orientation of S_{hmin} whereas DITFs are parallel to S_{Hmax} . Stress-induced failures in deep wells are some of the most reliable indicators of the S_{Hmax} orientation in the upper part of the crust. Stress-induced failures can be detected by tool measuring the borehole diameter in two directions (calipers), or by borehole image logs such as the Formation Micro Imager (FMI tm), a tool that scans the surface of the borehole with pads covered by tens of high-resolution electrodes. For this project, FMI is available from the interval 3473–3888 m MD, which includes part pre-Neogene basement of the Vienna Basin (Table 1). Bedding determined from FMI in the Furth Lst. and Werfen Fm. dips to WNW with mostly 20°–35°. A few small-scale faults are imaged in this interval,

in particular in the upper part of the Furth Lst. (Fig. 8). In the Gosau Group, bedding dips equally to WNW, but it is in general steeper, in particular below 3750 m, indicating intense deformation (Fig. 8).

The analysis of the FMI data shows that the contact between the Lower Triassic Werfen Fm. and the underlying Upper Cretaceous Gosau Group at 3694 m MD is formed by a fault oriented 250°/54° (Fault 1). The fault is marked by a dramatic change of tool response. It is associated with brecciation and two sub-parallel faults in the hanging wall and truncation of the bedding in the footwall (Fig. 9).

The analysis of stress-induced failures revealed no DITF in the study interval, whereas BO is relatively abundant (Fig. 8). In the Furth Lst., BO is observed in the upper 30 m, where four zones with a total length of 2.8 m are affected by compressive failures (Fig. 10A). In the Werfen Fm., only two small BO zones with a combined length of 0.85 m are interpreted (Fig. 10B). In the Gosau Group, in particular in the upper part, BO is very well developed covering a total length of 33.8 m (Fig. 10C, D).

In the Furth Lm. and Werfen Fm., the BO is consistently oriented, with features aligned close to E–W indicating that the S_{Hmax} is oriented close to N–S (Table 2). Even if the BO in the Furth Lst. and Werfen Fm. is rather short and small-sized their interpretation is sound. In fact, on the FMI these structures appear as symmetric areas 180° apart, with blurry appearance and conductive response, which is the typical appearance of BO on micro-resistivity image logs. In both formations, due to the rotation of the FMI tool during logging, the pads/flaps covered the entire areas affected by

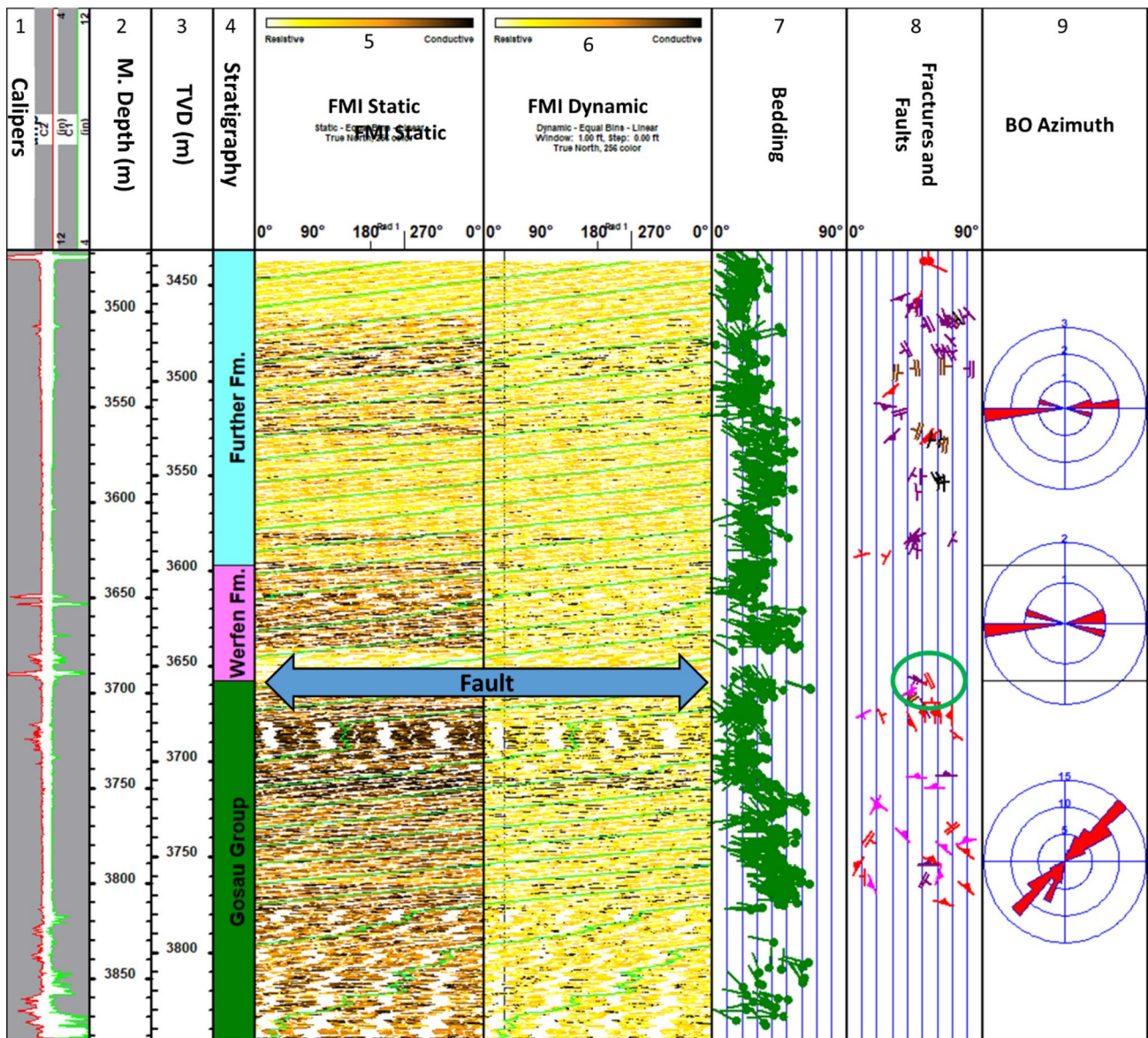


Fig. 8 Overview of the interval covered by the FMI data (3473–3888 m MD). Calipers are shown in tracks 1; Tracks 5–6 displays the static and dynamic FMI; Track 7 shows the tadpole track of the interpreted bedding (green symbols); Track 8 shows the orientation of

natural fractures (simple bar) and faults (double bar); Track 9 shows the azimuth of BO in the stratigraphic intervals shown in track 4. The position of the fault of Fig. 9 is shown on both the FMI images and the track 8 (green circle)

compressive failures, thus the azimuth of the BO in the two formations is fully constrained (Fig. 10A, B). Furthermore, as the intervals with BO in the Furth Lst. And Werfen Fm. Are about 150 m apart, the similar azimuth of the BO is a further confirm for the orientation of S_{Hmax} in the hangingwall of Fault 1. In the lower part of the Gosau Group, the BO is oriented SW-NE suggesting that S_{Hmax} is oriented close to NW–SE (Table 2). Data, therefore, indicate different stress orientation in the footwall and hanging wall of the fault mapped at the contact between the Triassic formations and the Gosau Group below.

1D geomechanical model

Overburden stress (S_v), mud pressure and pore pressure

Prior to the estimation of the geomechanical model a preliminary analysis was performed to identify the major lithological boundaries in the well from available data (FMI, OHL, mud log, and drilling report). The Miocene Vienna Basin fill is mostly dominated by silty marls and shales, with minor sandstones and conglomerates, whereas in the

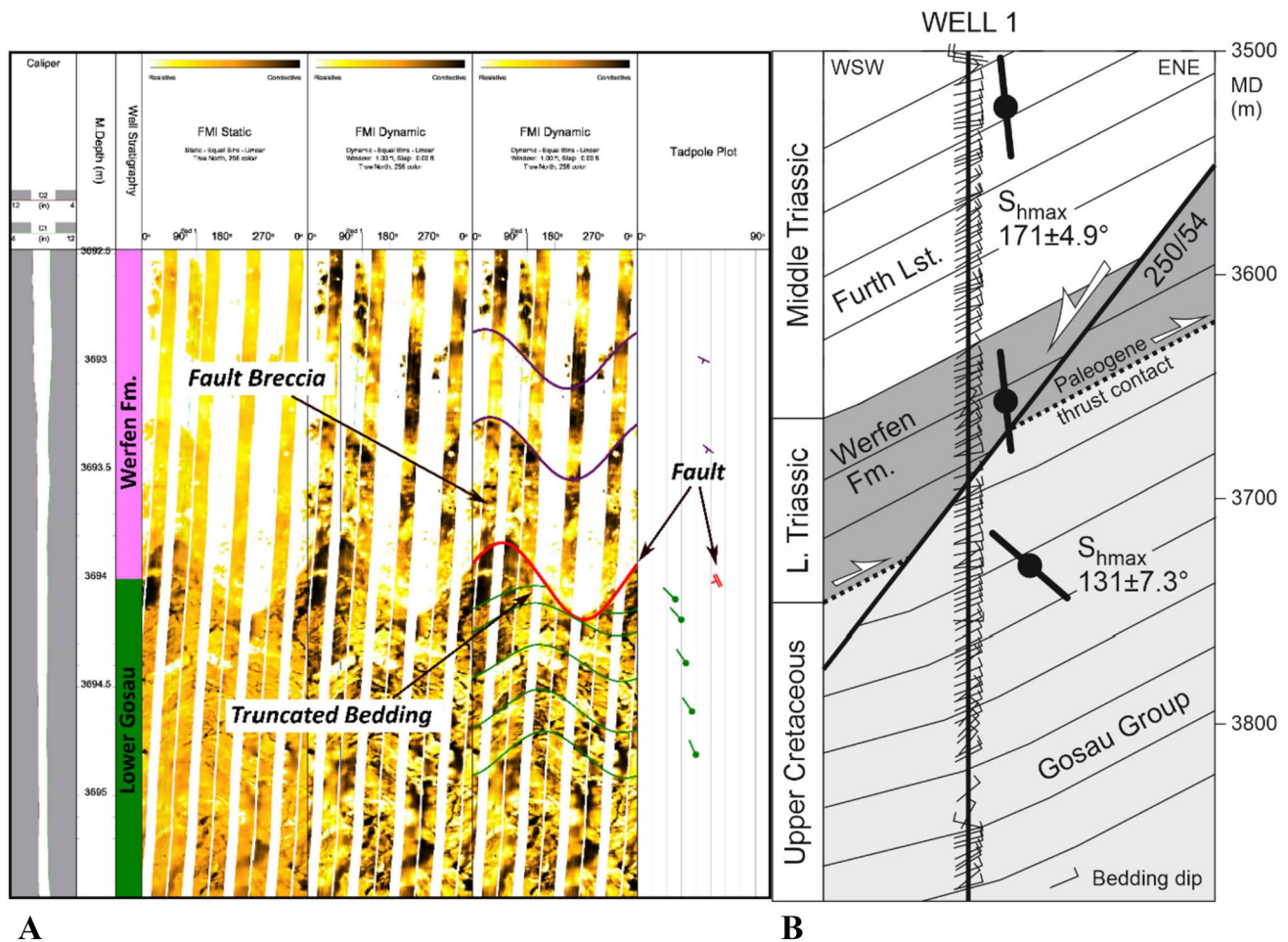


Fig. 9 **A** FMI data covering the contact between lower Triassic Werfen Fm. and upper Cretaceous Gosau Group. Data shows a ESE-dipping fault (250/54) between the two formations at 3694 m MD (corresponding to 3657.8 m TVD). Note the brecciated texture in the hanging wall and truncated bedding in footwall. Two additional sub-parallel faults are interpreted in the hanging wall between about

3693.0 and 3693.5 m MD. Red sinusoids and tadpole: fault; purple: faults in hanging wall; green: bedding **B** Near-well profile of Well 1 in the interval 3500–3900 m MD covering the fault at 3694 m MD between Werfen Fm. and Gosau Group. Bedding dips are based on FMI data. The cross-section is oriented perpendicular to the fault strike, projected dips have been decimated

basement limestones are also present. Due to the lack of shear wave data, a synthetic shear-wave sonic log (DTS) was extrapolated from the compressional sonic log (DTC), based on a fixed relationship, which in sandstones and shales was derived from Castagna et al. (1985) (Eq. 1):

$$V_s = 0.804V_p - 0.856 \text{ (km/s)}. \quad (1)$$

The relationship was used for the complete Miocene section, the Werfen Fm. and Gosau Group. For the limestones of the Furth Lst., V_s was extrapolated according to Castagna et al. (1993) (Eq. 2):

$$V_s = -0.055V_p^2 + 1.017V_p - 1.031 \text{ (km/s)}. \quad (2)$$

The magnitude of the overburden stress (S_v) was calculated using the relationship (Eq. 3):

$$S_v = \int_0^z \rho(z)g dz \quad (3)$$

where ρ is the density determined from the density log (RHOZ), z the true vertical depth and g the gravitational acceleration (Zoback 2007). As no density correction curve was provided, the raw density curve (RHOW) was used for the vertical stress modeling after removing intervals with obvious poor data that might have introduced some potential error for the intervals in which the density log readings might have been affected by poor logging. For the top-hole interval (0–750 m) a constant density of 2.1 g/cm³ was assumed based on the average measurements in the upper part covered by the OHL, where Pannonian sediments occur, as in the majority of the remaining part of the upper part of the borehole (Fig. 5). No data were available in literature or

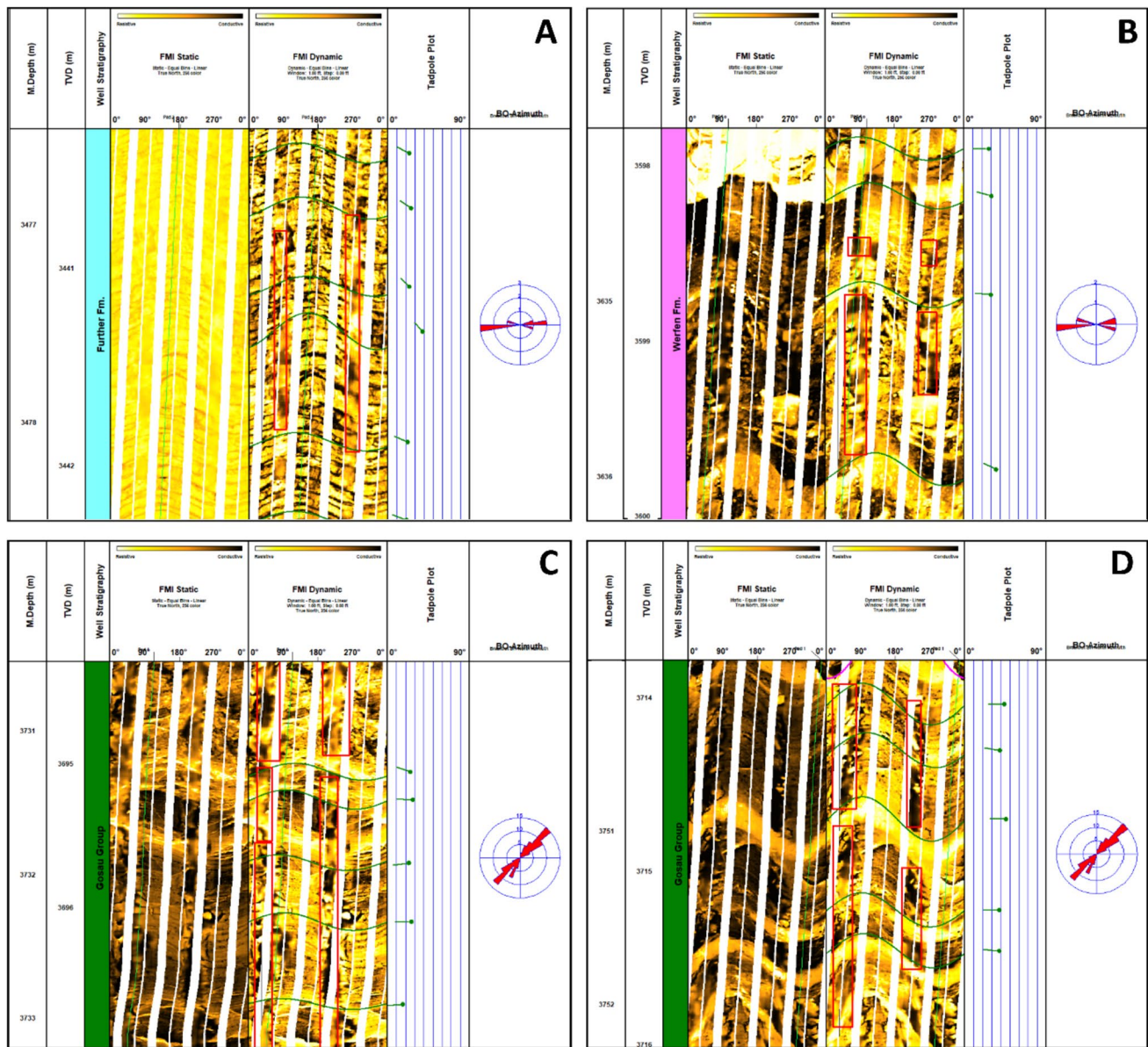


Fig. 10 Instances of borehole breakout in different intervals of Well 1 and corresponding BO azimuths shown in stereonets in the right part of each figure. **A, B:** E-W oriented BO in Furth Lst. and Werfen

Fm. **C, D** SW-NE oriented BO interpreted in the Gosau Group. Green sinusoids and tadpoles denote bedding; red boxes highlight BO

Table 2 BO observed in the stratigraphic intervals covered by FMI data of Well 1 and the corresponding inferred orientation of the S_{Hmax}

Top (m)	Bottom (m)	Stratigraphy	BO zones no	Total length (m)	S_{Hmax} (azimuth)
3397	3633	Furth Lst	4	2.8	$174^{\circ} \pm 4.9^{\circ}$
3633	3694	Werfen Fm	2	0.85	
3694	4224	Gosau Group	40	33.8	$131^{\circ} \pm 7.3^{\circ}$

DITFs are not observed at any depth

from nearby boreholes covering the upper part of the Vienna Basin succession (at the moment in Austria there is no open database for borehole logs). This may have caused a potential over-estimation of S_{IV} in the upper part of the well that

can be estimated between 0.74 and 1.47 MPa (at 750 m), for densities in the range 2.0 and 1.9 g/cm³. For the interval not covered by open hole logs (3166–3362 m MD) density was extrapolated from the first reliable data recorded above

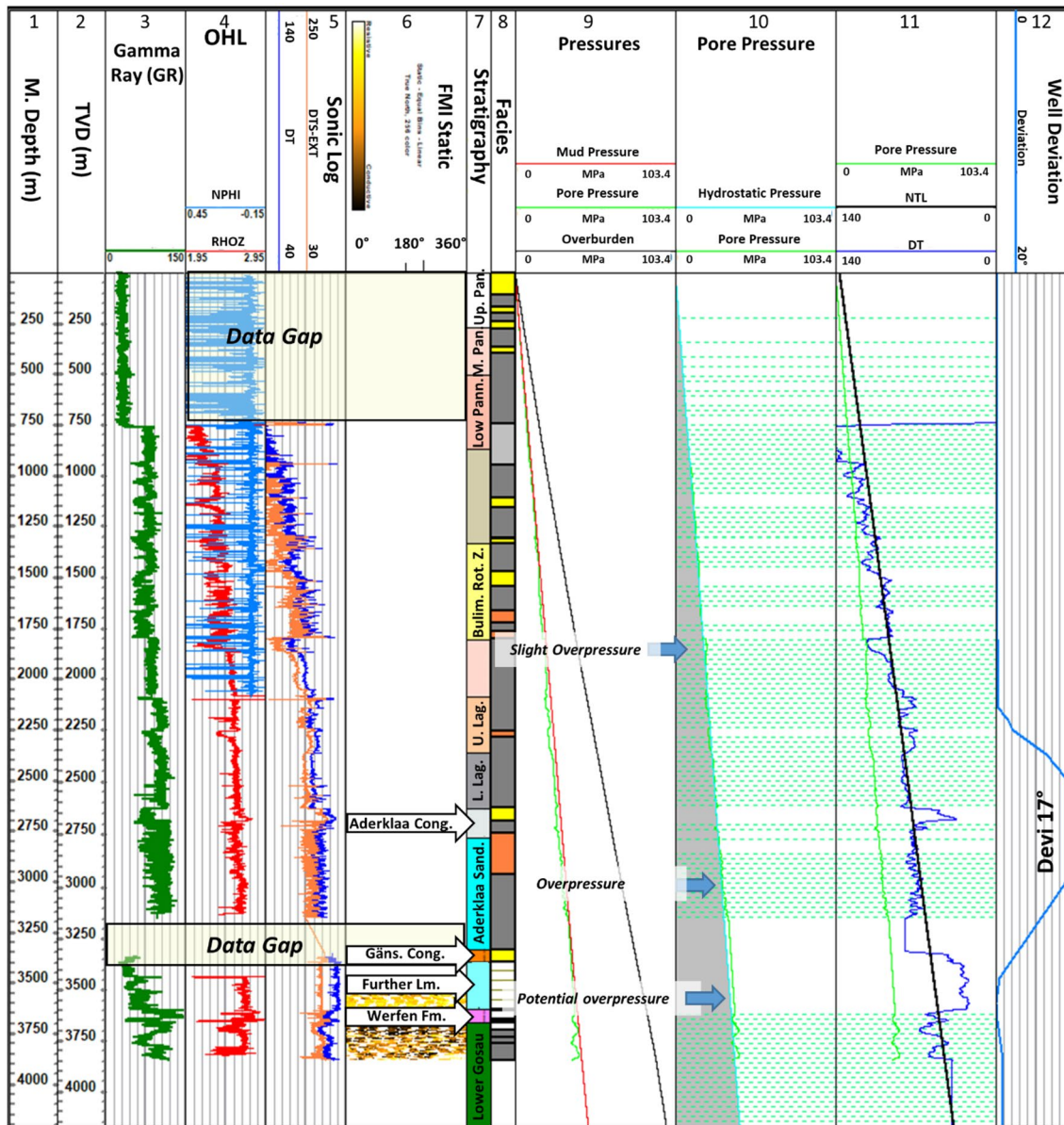


Fig. 11 Open hole logs (OHL) of Well 1 (track 3–5), computed overburden stress, mud pressure and pore pressure (tracks 9 to 11). Track 3: gamma ray; Track 4: density (red, RHOZ) and neutron porosity (blue NPHI); Track 5: compressional (blue DT) and estimated shear (orange DTS-Ext) sonic slowness; Track 7–8 display the well stratigraphy and corresponding lithofacies. Track 9 shows pore pressure (green curve) mud pressure (red curve) and overburden stress (black

curve). Track 10 shows the pore pressure (green curve) plotted over the hydrostatic pore pressure (light blue curve). Track 11 displays the shale intervals (green dashed lines), the reference sonic log (blue) and the normal trend line (black) used for the Eaton’s formula. DT: sonic log; NTL: normal compaction trend line. For the facies (Track 8) the following color coding was used: yellow conglomerate, orange sandstone, dark gray silt and light gray shale

and below the interval. The mud pressure (MP) at depth was computed from the mud weight profile derived from the daily reports (Fig. 5) and assuming a static pressure generated by the hydrostatic column at the given true vertical depth. An overview of the computed overburden stress (S_v) and mud pressure is shown in Fig. 11 (track 9).

The pore pressure profile was estimated with the Eaton’s (1975) method based on the assumption that in shaly lithologies the overburden stress (S_v) generates progressive compaction with depth, which is associated with a loss of porosity. The trend is frequently observed in sonic logs showing increasing velocities with depth. A drop of sonic velocity from the normal trend is typically interpreted to reflect

overpressured sediments. The method of Eaton (1975) is based on the difference between the compaction trend, or normal trend line (NTL), and the sonic log (DT) (Eq. 4):

$$P_o(\text{shales}) = S_v \times (1 - wt) + H_p \times wt. \quad (4)$$

With P_o (shales): pore pressure in the shales; S_v : overburden stress; H_p : Hydrostatic Pore Pressure; $wt = (DT/NTL)^n$; n is an adjustable exponent. After the identification of the shale intervals, based on the indications from both mud-log and open hole log data, a normal compaction trend line (NTL) was defined on the sonic log (DT) (tracks 10–11 of Fig. 11). The base of normal pressure was set at 950 m, whereas below that the pore pressure in the shales was estimated using the Eaton's equation (Eq. 4), setting the exponent n to 0.5. In permeable sections confined within shales the pore pressure was estimated from the values in the shales above and below and assuming hydraulic continuity. Approximating the pore pressure with the Eaton's method in the pre-Neogene basement of the Vienna Basin below 3397 m (MD) was particularly problematic due to a gap of sonic data between 3170 and 3370 m (MD) and due to the fact that shales of the Werfen Fm. and Gosau Group preserve an older compaction history. Lacking any direct pore pressure in the study well and in nearby boreholes, there are no data for a direct validation of the modeled pore pressure. Only the daily drilling reports and the described equilibrium with static mud pressures can be used to provide some constraints for the pore pressure estimation. In the upper part of the borehole, represented by the Miocene Vienna Basin fill (11–3397 m), the lack of kicks or mud losses during drilling indicates that the chosen mud density (close to 1.12 g/cm³) was adequate to cope with the encountered pore pressure (Fig. 6). This evidence agrees with the estimated pore pressure close to hydrostatic conditions over most of the interval with the onset of moderate overpressure in the Aderklaa Fm. (tracks 9–10 of Fig. 11). In the pre-Miocene basement drilling required a mud density significantly higher than in the basin infill, which was initially close to 1.22–1.24 g/cm³ and later even higher 1.25–1.26 g/cm³ (Fig. 6). The lack of both kicks and mud losses in this section indicates drilling parameters (relatively high mud pressure) close to balance, which strongly supports overpressured conditions.

Rock properties

The rock properties were extrapolated from existing geophysical logs, using well established empiric correlations (for a review see Chang et al. 2006). Curves with obviously wrong values have been discharged in a preliminary quality control phase, mostly at the top and bottom of the logged intervals. However, small-scale spikes in some of

the OHL curves, mostly resulting from poor borehole condition or logging, were not corrected, resulting in local spikes also in the estimated properties. In the upper part of the section with OHL, a few spurious curves resulted from poor logs at the very top, that did not affect the geomechanical model (Fig. 14). In the shales, the unconfined compressive strength (UCS) was estimated with the Lal (1999) equation (Eq. 5):

$$\text{UCS (MPa)} = 10(304.8/\Delta t - 1) \quad (5)$$

where Δt is the interval transit time $\Delta t = V_p^{-1}$ ($V_p = P$ -wave velocity). In the various carbonatic lithologies present in the well, Militzer's (1973) formula was used (Eq. 6):

$$\text{UCS (MPa)} = (7682/\Delta t)^{1.82}/145 \quad (6)$$

In sandstones and conglomerates, the unconfined compressive strength was estimated with the formula of Moos et al. (1999) (Eq. 7):

$$\text{UCS (MPa)} = 1.745 * 10^{-9} \rho V_p^2 - 21 \quad (7)$$

With Δt : transit time; ρ : density; V_p : P-wave velocity. After the calculations, the curves were merged and smoothed, to correct high frequency fluctuations resulting from the input curves (track 9 of Fig. 12).

The coefficient of internal friction (μI) was estimated from V_p (P-wave velocity) with the empirical formula proposed by Lal (1999) (Eq. 8):

$$\mu I = \tan [\sin^{-1}(V_p - 1)(V_p + 1)] \quad (8)$$

This formula was originally proposed for shales but proved to work well also for other shaly sedimentary rocks, thus it was used also for marls. In the clean limestones characterizing the Further Lst., for which no empirical formula can be used, a fixed value of 0.8 was used. The smoothed estimated coefficient of friction can be seen in track 10 of Fig. 12.

Compressional and shear wave velocities (V_p and V_s) of the sonic logs (DT and DTS) were used to calculate the dynamic Poisson's ratio (ν) using the formula (Eq. 9):

$$\nu = (V_p^2 - 2V_s^2)/2(V_p^2 - V_s^2) \quad (9)$$

Due to coverage of the sonic logs, reasonable Poisson's ratio estimations are available for the intervals 740–3174 m and 3374–3876 m (MD). The Poisson's ratio in combination with V_s and the density measurements (ρ) of the density log (RHOZ) was further used to estimate the shear modulus (G-MOD), using the relationship (Eq. 10):

$$V_s = \left(\frac{G}{\rho} \right)^{1/2} \quad (10)$$

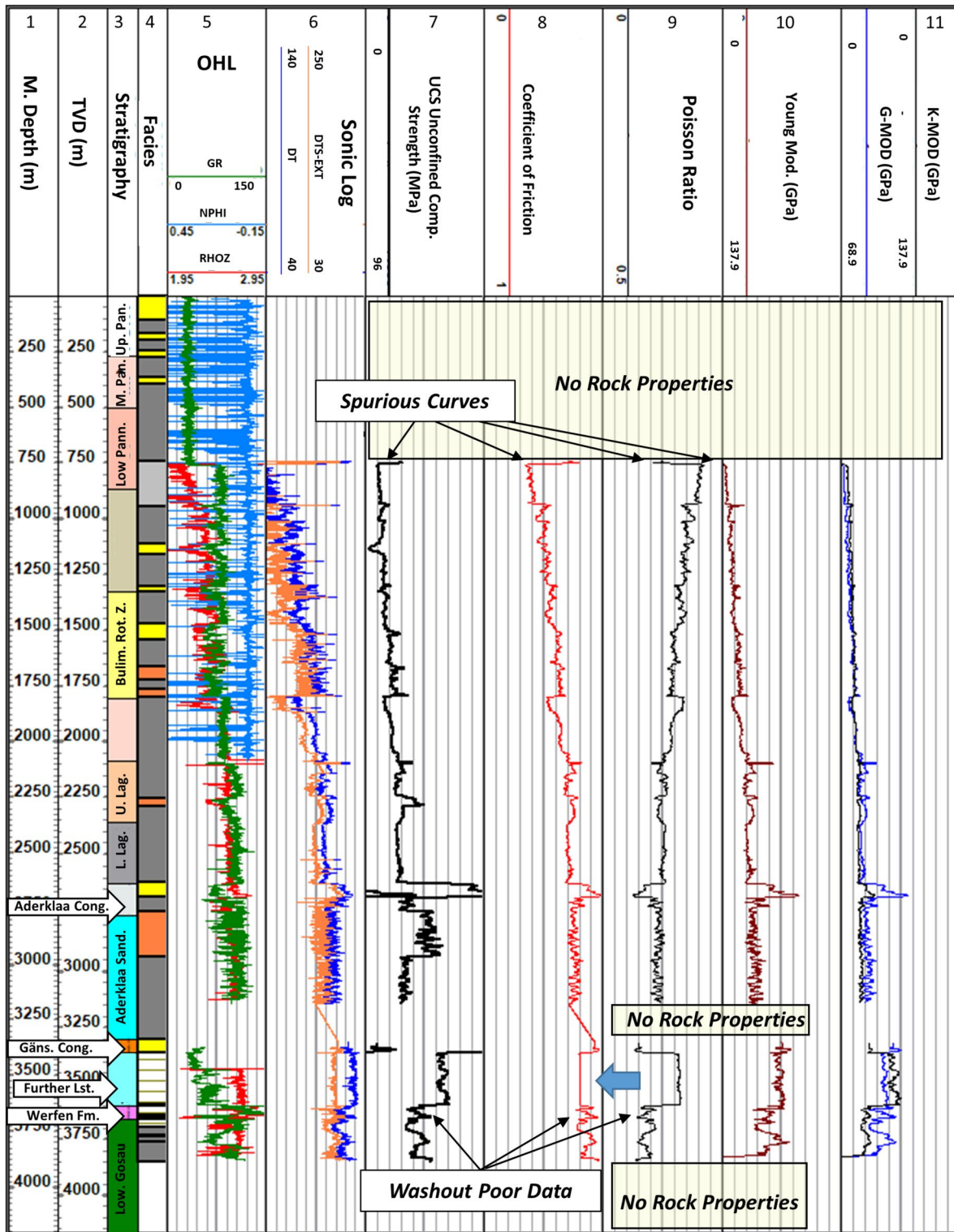


Fig. 12 Open hole logs (OHL; tracks 3–5), calculated rock properties and dynamic elastic moduli (tracks 9–13). OHL track 3: gamma ray; 4: density (red) and Neutron porosity (blue); 5: sonic with Vs (blue) and calculated Vs (orange). Calculated rock properties track 9: unconfined compressive strength (UCS); 10: coefficient of friction (μ); 11: dynamic Poisson ratio; 12: dynamic Young’s modulus;

13, dynamic shear modulus (G-MOD) and dynamic bulk modulus (K-MOD). In the upper part of the well, just below the interval with no OHL, several spurious data are present, resulting from poor logging, that are not considered in the model. For the facies (track 8) the following color coding was used: yellow conglomerate, orange sandstone, dark gray silt and light gray shale

The dynamic Young (E) and Bulk (K -MOD) moduli were inferred from shear modulus and Poisson’s ratio using well established relationships (Zoback 2007). The resulting curves have been manually edited in intervals with severe borehole rugosity and smoothed to remove high frequency spikes derived from both sonic and density logs. Smoothed dynamic elastic moduli can be seen in tracks 11–13 of Fig. 12.

The dynamic Young modulus (E) was converted to the static equivalent using one of the linear relations reported by Wang (2000) (Eq. 11):

$$E_{\text{stat}} \text{ (GPa)} = 0.41(E_{\text{dyn}}) - 1.06 \tag{11}$$

Ideally, the dynamic-static conversion of the Poisson’s ratio should be performed using the results of tested cores in the same formation, and use basic correlations against dynamic values to apply a correction. However, no cores were retrieved in Well 1. The dynamic–static conversion of the Poisson’s ratio is a rather problematic procedure, as there are not many published correlations in literature that can be considered valid in other settings, as they tend to provide locally relationships but that are sometimes not univocal and difficult to extrapolate to other settings (Blake et al. 2019, 2020; Yang et al. 2022). This issue is discussed in detail in Blake et al. (2020), in which they combine results of new tests with available data in literature, summarized in their Fig. 12. This overview of old and new data indicates relatively scattered distribution, even with some significant outliers. However, a low-confidence correlation can be inferred suggesting that, lacking any better data, we can estimate that (Eq. 12):

$$\nu_{\text{stat}} = 0.75\nu_{\text{dyn}} \tag{12}$$

Most of the estimated rock properties have been slightly smoothed, to mitigate the effects of the above mentioned high-frequency spikes resulting from poor borehole condition or logging. The only interval in which no improvement was achieved is the washout zone in the lower part of the Werfen Fm., in which the rock properties are poorly estimated over a longer interval, which is highlighted in Fig. 12.

Stress polygons

Stress polygons allow evaluating the field of potential stress magnitudes at a given depth, corresponding to specific pore pressure, overburden stress (S_v) and coefficient of friction (μ). As the coefficient of friction of faults (μ) is in general comprised between 0.6 and 0.8, two sets of stress polygons were made, using the two values. The external limits of the stress polygons are estimated assuming a Mohr–Coulomb failure criterion, whereas the internal boundaries identify the three Andersonian stress regimes: normal-faulting (NF),

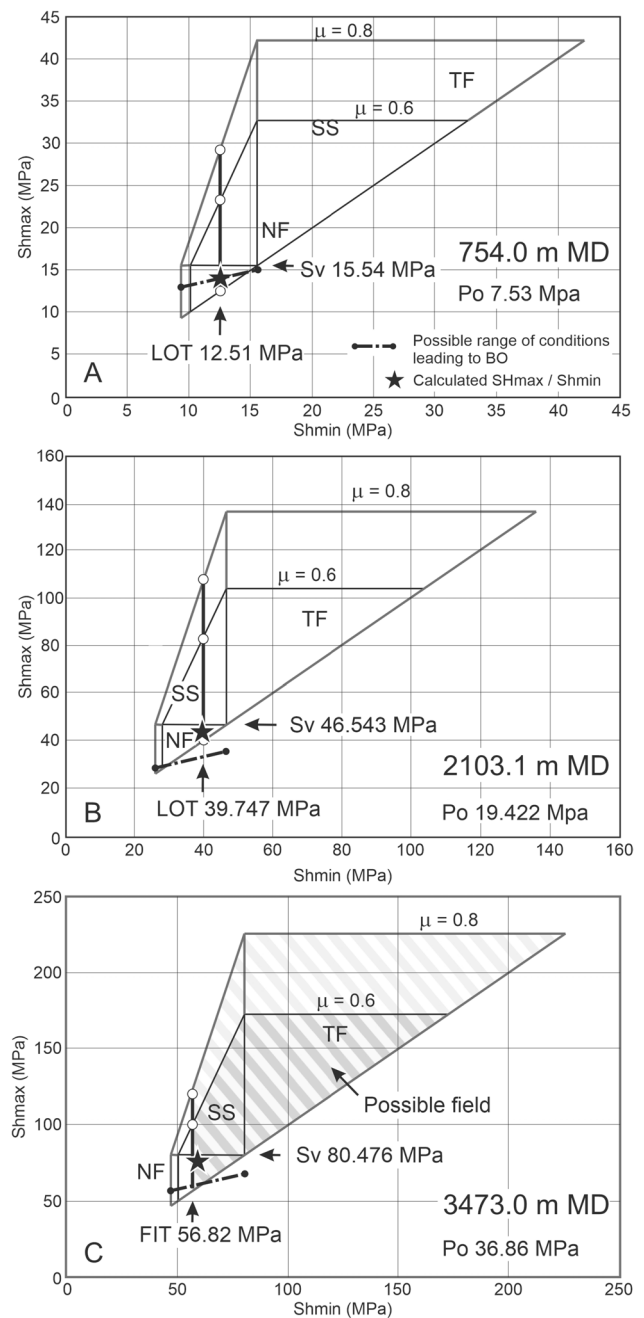


Fig. 13 Stress polygons for the two leak-off tests (LOT) at 754.0 m (A) and 2103.1 m (B), and the formation integrity test (FIT) at 3473.0 m depth (C). The conditions for the development of BO in the borehole wall based on Eq. 15 are also plotted. Black stars represent the magnitudes of the modeled S_{hmin} and S_{Hmax} . Bold vertical lines in (A) and (B) represent the range of potential S_{Hmax} magnitudes for the given friction coefficients (μ) (0.6 or 0.8), S_v and S_{hmin} from the LOTs. C FIT provides only a lower bound magnitude for S_{hmin} . The field of possible horizontal stresses is therefore much larger than in (A) and (B) NF: normal-faulting; SS strike-slip; TF thrust faulting

strike-slip (SS) and thrust faulting (TF). Any point near to the limits inside of the polygon represents a stress field close to critically stressed conditions, with a suitable oriented fault

close to slip (Moos and Zoback 1990; Zoback 2007). Leak-off tests (LOT) provide an estimation of the S_{hmin} magnitude, thus on the stress polygons, these data are plotted as a vertical line delimiting the values of all the possible S_{Hmax} magnitudes corresponding to a given magnitude of S_{hmin} to that line.

The stress polygons corresponding to the two leak-off tests at 754 and 2103.1 m MD (at this depth MD is equal to TVD) indicate that at both depths the stress regime is normal-faulting or strike-slip (Fig. 13). Moreover, both stress polygons represent rather stable conditions for both coefficients of friction, with the critical conditions expected only at the upper limit of the strike-slip regime and with very high S_{Hmax} magnitudes (arrows in Fig. 13). For the Mesozoic units at 3473.1 m MD (3399.9 m TVD), the stress polygon indicates a much larger field of potentially possible stress magnitudes as the formation integrity test (FIT) does not provide a close estimation of the S_{hmin} magnitude but just constrains its lower boundary (Fig. 13).

Horizontal stresses

The two LOT in the upper part of the borehole could be used to estimate the S_{hmin} at depth by computing the corresponding gradients and extrapolating them to depth. At 754 m (MD = TVD), the computed gradient is 16.60 MPa/km, whereas at 2103.1 m (MD = TVD) the gradient is 18.90 MPa/km. Thus, there is a difference of about 2.3 MPa/Km (13.8% of the gradient at 754 m). Using the two gradients to estimate S_{hmin} at the depths of the FIT (3474.1 m MD; 3399.9 m TVD) would result in a magnitude of S_{hmin} between 56.44 and 64.26 MPa, with a difference of about 7.8 MPa (about 13.8%). The estimate derived using the gradient at 754 m (16.60 MPa/km) is rather close to the value of the FIT (56.82 MPa). However, using the deeper and closer gradient would appear more advisable. Furthermore, the two LOT are from intervals in which the pore pressure has similar gradients (close to hydrostatic), whereas the lower part of Well 1, below 3000 m, is characterized by increasing overpressure (Fig. 11), which might also affect the S_{hmin} gradient at depth. For these reasons we concluded that estimating the S_{hmin} magnitude at depth with a constant gradient was not the best option.

Instead, the estimation of the magnitudes of the two horizontal stresses (S_{Hmax} and S_{hmin}) was performed with the following poroelasticity model with the Biot's coefficient set to 1 (Eqs. 13, 14):

$$S_{\text{hmin}} = [v/(1-v)] * (S_v - P_o) + P_o + [(v * E)/(1-v)]\epsilon x + [(E)/(1-v)]\epsilon y \quad (13)$$

$$S_{\text{Hmax}} = [v/(1-v)] * (S_v - P_o) + P_o + [(v * E)/(1-v)]\epsilon y + [(E)/(1-v)]\epsilon x \quad (14)$$

With ν Poisson's ratio (static), P_o pore pressure, E Young's modulus (static), ϵx and ϵy two adjustable parameters to account for the tectonic component. This method to estimate the stress field at depth is rather well known and has been successfully used in many studies in various geologic setting (Najibi et al. 2017; Radwan and Sen 2021a, b; Leila et al. 2021), including also areas with expected active faulting (Alam et al. 2019). In the 1D model of Well 1, the two parameters ϵx and ϵy were used dynamically with depth, also to account for the uncertainties in the estimation of the static E Young's modulus and in particular the ν Poisson's ratio. To evaluate the impact of potential error due to a wrong dynamic-static conversion of the Poisson's ratio (see Eq. 12), various other scenarios were tested resulting in slightly different stress magnitudes. If the dynamic-static correlation is in between 0.5 and 1, the model would predict stress magnitudes that increase by 1.7 and 1.8 MPa, or drop for about 1.5 and 1.6 MPa at 2103.1 m MD (depth of the LOT). This indicates maximum error in the range of $\pm 3.7/4.2\%$. As the estimated rock properties include some high-frequency spikes derived from poor quality of the curves used to derived them (density and sonic logs), these propagate also in the estimation of the magnitudes of S_{hmin} and S_{Hmax} . The intervals with poor prediction of the stress magnitudes resulting from significant issues in the estimated rock properties are highlighted in the figures.

The two parameters ϵx and ϵy are first edited to fit the magnitude of S_{hmin} at the available LOT, assuming that it is the smallest stress (σ_3). Subsequently, the two constants are interactively edited to generate stress magnitudes that fit the observed borehole conditions. A validation is performed by comparing the borehole stability predicted by the model for the given mechanical system, borehole orientation and drilling parameters, and the actual drilling experience and borehole conditions. The method is very similar to the procedure originally proposed by Zoback et al. (2003) but uses slightly different equations for the stability analysis. The conditions for the development of BO in the borehole are defined based on the hoop stress at the borehole wall in the sectors with the maximum concentration (see Eq. 6.8 of Zoback 2007) and assuming a linearized Mohr–Coulomb criterion. This results in the equation below defining the conditions for a compressive failures of the borehole wall (Eq. 15):

$$S_{\text{Hmax}} = ((S_{\text{hmin}} + \text{UCS} - P_o(q - 1) + M_p(q + 1))/3) \quad (15)$$

With M_p : mud pressure and q is from Eq. 4.7 of Zoback (2007) and (μI) is coefficient of internal friction estimated with Eq. 8 (Eq. 16):

$$q = \left(\sqrt{\mu I^2 + 1} + \mu I \right)^2. \quad (16)$$

The validation is performed calculating two hypothetical mud weight curves for drilling the borehole with no borehole breakout (curve Min-MUD) (Eq. 15) and no DITF (curve Max-MUD), respectively. These hypothetical curves are then compared to the actual mud weight used to drill the borehole (curve Mud-Weight). Intervals where the geomechanical model predicts the development of borehole breakouts should be characterized by Mud-Weight < Min-MUD, whereas tensile failures should occur where Mud-Weight > Max-MUD. In this wellbore stability analysis, in intervals with predicted BO, thus where Mud-Weight < Min-MUD, the larger the separation between the curves, the more intense are the compressive failures going to be, providing also a tool to estimate also the BO width. The model is adjusted until a good match between predicted and observed failures is reached.

In the upper part of the well (750–3473 m MD), ϵ_x and ϵ_y were first adjusted to match the magnitude of S_{hmin} with the values of the two leak-off tests at 754.0 and 2103.1 m MD depth and subsequently interpolated (track 7 of Fig. 14). Plotting on the stress polygons, the lines corresponding to the conditions for generating BO in the borehole as defined by Eq. 15 can provide some further constrains for the modeling. At 754 m MD the well might develop BO if the S_{Hmax} is more than 13.8 MPa. Unfortunately, in the 17.5 in section (750–2090 m MD), only one un-oriented caliper curve is available, measuring the borehole diameters along two opposite arms (curve BD-1), which shows some enlarged sections that might be either BO or any other sort of borehole enlargements. The modeled S_{Hmax} at this depth lies very close to the line for the development of BO (Fig. 13a). However, there is no caliper data supporting that assumption. The model predicts BO development and no DITF over the lower part of the 17.5 in section as indicated by Mud-Weight < Min-MUD and Mud-Weight < Max-MUD (Fig. 14). Some of the enlargements detected by the individual caliper correlate to some of the predicted BO by the model, but should not be considered a good validation (track 9 Fig. 14).

In the 12.25 in section (2100–3179 m MD), there are three sets of un-oriented caliper curves (HD-1, HD-2, HD-3) measuring the borehole diameter between 3 sets of opposite arms, originally logged with a 6 arms tool (track 9 of Fig. 14). Thus, intervals where two curves are on gauge (compared with bit size curve: BS) and one is over-gauged are almost certain BO. However, lacking the orientation

curves BO cannot be fully confirmed. The stress polygon at 2103.1 m shows that there are no possible ranges of S_{Hmax} that can avoid the development of BO (Fig. 13). The modeled magnitude of S_{Hmax} at 2103.1 m fits within the limits of the stress polygon for both 0.6 and 0.8 coefficient of friction (Fig. 13b). The BO predicted by the data plotted on the stress polygon agrees with the observed abundant potential breakouts in interval just below the LOT (track 9 Fig. 14). In the entire 12.25 in section, several intervals display good match between the modeled BO and the potential BO detected by the calipers (2100–2600 m; at 2750 m).

In the lower part of the borehole (3473–3888 m) the less accurate formation integrity test (FIT) limited the level of confidence of the estimated S_{hmin} value, as shown by the stress polygon (Fig. 13). The conditions for BO indicate that almost any magnitude of S_{Hmax} (greater than the FIT) would lead to BO, except for only a small interval with S_{Hmax} close to S_{hmin} that would be stable. The modeled stress magnitudes at 3473 m MD indicate that S_{hmin} is greater than the FIT (as it should be), whereas S_{Hmax} is rather close to the transition to strike-slip. These conditions plot in the field in which BO cannot be avoided (Fig. 13c). FMI data covering the depth between 3373 and 3884 m MD allow a detailed validation of the 1D geomechanical model by comparing of model predicted and observed failures. The FMI data show no DITF and little borehole breakout in the Furth Lst. and Werfen Fm., whereas in the upper part of the Lower Gosau BO is very intense (track 12, Fig. 15). In the lower part of the Lower Gosau, the borehole diameter is badly out of gauge, indicating a potential collapse, which agrees with the repeated reaming attempted in this section to keep the borehole open. In the lower section, the 1D model is compatible with the results of the FMI data as indicated by the curve Min-MUD > Mud-Weight mostly in the intervals where borehole breakout is observed on the FMI, and the curve Max-MUD > Mud-Weight over the entire interval (excepted sections with poor data, due to borehole enlargements) (tracks 11–12, Fig. 15). Moreover, the azimuth borehole breakout rotates from E–W to SW–NE at the bottom of the Werfen Fm., where a fault was interpreted (track 7, Fig. 15). Below the Furth Lst both stress magnitudes show significant variations, due to varying elastic moduli, which in part result from poor borehole conditions affecting the sonic logs. An interval with poor stress estimation occurs in the lower part of the Werfen Fm., in which a long washout occurs, which affected the estimation of the rock properties (Fig. 15).

Seismic data

Integration of Well 1 data with 3D seismic shows that the well penetrates five WSW-dipping normal faults of the AFS

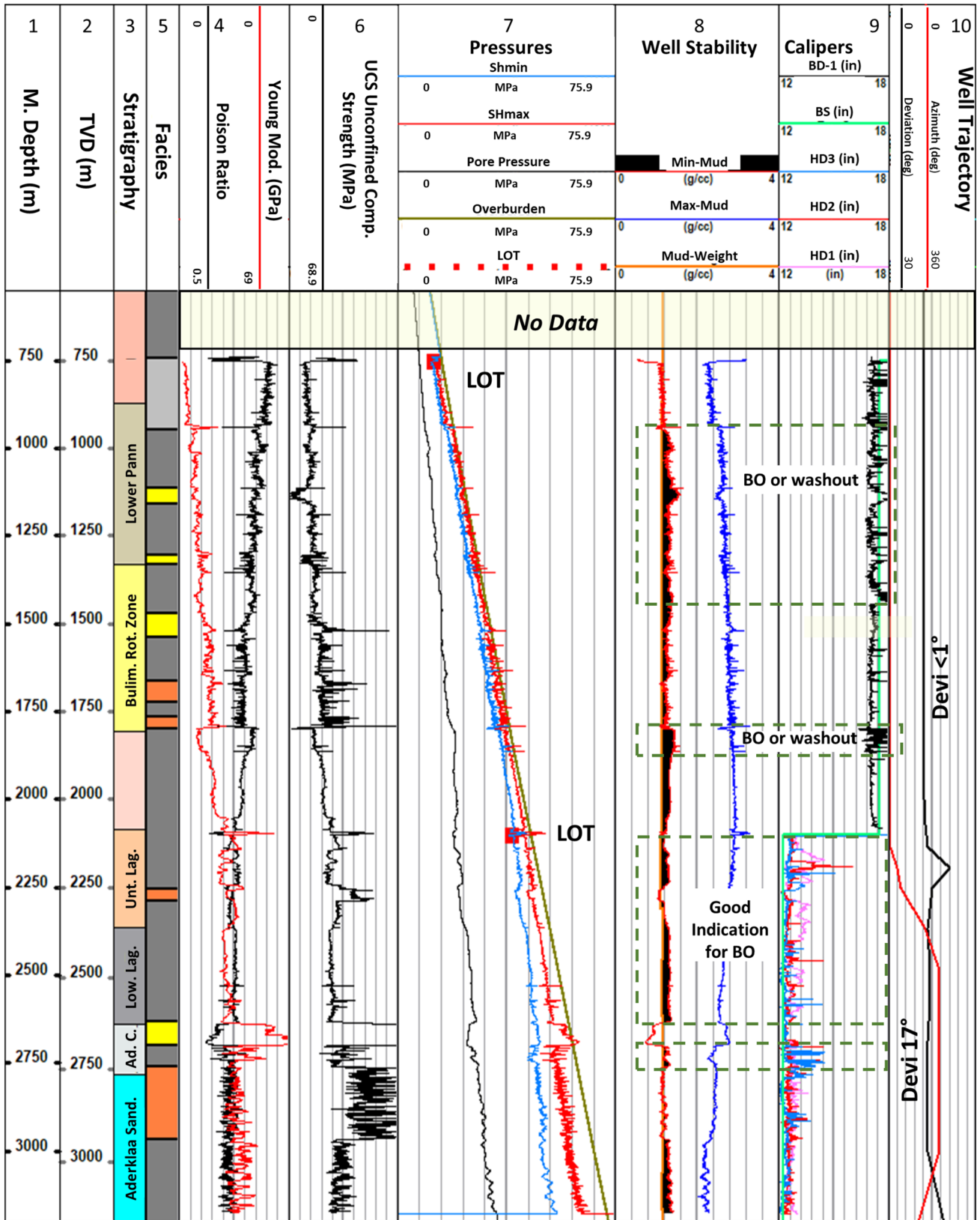


Fig. 14 1D geomechanical model in upper part of Well 1 (750–3170 m MD). Stress magnitudes are plotted in track 7 together with pore pressure and the leak off tests (LOT). Below about 1500 m MD the model indicates normal faulting with $S_v > S_{Hmax} > S_{Hmin}$. Olive: S_v ; red: S_{Hmax} ; blue: S_{Hmin} ; black: pore pressure. Track 8 shows the well stability analysis with the Min-MUD curve (red) and Max-MUD curve (blue) plotted against the actual mud density (Mud-Weight curve). In track 9 the bit size (BS) is plotted against not oriented calipers. In the 17.5 in section (750–2090 m) only one curve (BD-1) is available, measuring the borehole diameter between two opposite arms, which allows the identification of borehole enlargements that could be BO or washout. In the 12.25 in section (2100–3179 m) three curves occur, measuring the diameter along 3 sets of opposite arms of a 6 arm tool (HD1, HD2, and HD3). These curves allow a much better identification of potential BO in interval σ with two curve close to BS and one over-gauge. Green boxes indicate intervals in which the model predicts BO, that partially correlate to potential BO detected by the caliper data. For the facies (track 5) the following color coding was used: yellow conglomerate, orange sandstone, dark gray silt and light gray shale

(Fig. 16). Faults are reliably mapped in the Miocene sediments above the band of strong reflectors of the Aderklaa conglomerate between about 2300 and 2500 m depth. Below these reflectors seismic quality falls off progressively and is particularly low in the pre-Neogene basement belonging to the Northern Calcareous Alps, probably due to intense faulting and the frequent occurrence of steep reflectors. Terminations of short continuous reflectors, however, allow mapping the downward continuations of faults below the Aderklaa reflectors with sufficient accuracy. Horizon maps and time slices of the 3D seismic show that the faults of the AFS are strongly non-planar showing SSW–NNE strikes and WNW-directed dip in the N, and a progressive rotation of fault strike to WNW–ESE and dip towards WSW next to Well 1 (Fig. 17). Seismic data further show that in the WNW–ESE striking part of the AFS is represented by a system of closely spaced faults rather than one single structure. Well 1 penetrates WSW-dipping normal faults between about 2000 and 3500 m depth below sea level (Fig. 16). The maximum normal fault offset of about 100 m is observed at fault A5 within the Aderklaa Fm. (ca. 2650 m below sea level). The fault at the contact Werfen Fm. / Gosau Group in 3694 m MD of Well 1 (compute TVD 3656.8 m) (Fig. 8) is correlated to Fault 1 in the seismic, which is part of an array of three sub-parallel faults cutting the borehole between about 3200 and 3600 m depth.

Discussion

Fault 1 (3694 m) interpreted on the FMI data of Well 1 between the Werfen Fm. and Gosau Group strikes NNW–SSE and dips to the WSW with 54° . The FMI mapped fault is, therefore, sub-parallel to the nearby segment of the AFS (Figs. 8, 17). Even if the kinematics of

Fault 1 cannot be inferred from the analysis of the FMI data, the structural data and the presence of older formations in the hanging wall suggests that it can be regarded as a normal fault cutting through an older thrust, which brought the Lower Triassic Werfen Fm. on the Upper Cretaceous Gosau Group. 3D seismic shows that the fault is part of the AFS, which consists of several WSW-dipping seismic-scale normal faults. In the hanging wall of Fault 1 the orientation of BO, even if it is represented by relatively few data, indicates that the S_{Hmax} is oriented close to N-S, whereas in the footwall abundant BO indicates that S_{Hmax} is oriented NW–SE, i.e., parallel to the strike of the normal fault (Figs. 8, 9). Progressive rotations of the in-situ stress in an active fault zones have been interpreted as resulting from stress perturbations, generated by stress release trough fault slip (Barton and Zoback 1994; Brudy et al. 1997; Zoback et al. 2003; Pierdomenici et al. 2011; Alam et al. 2019; Levi et al. 2021), whereas different stress orientations preserved in independent tectonic blocks separated by active faults have been interpreted as stress decoupling (Reinecker and Lenhardt 1999; Jarosinski 1998). The observed stress rotation at fault 1 in Well 1, therefore, strongly indicates that the drilled branch fault of the AFS should be regarded as potentially active. In the Vienna Basin, similar stress rotations associated to active faulting have also been observed in several other deep wells and interpreted to indicate active faults (Marsch et al. 1990; Decker and Burmester 2008). The fact that Fault 1 is capable of interfering with local stress field is an indication of tectonic activity which suggests that this part of the AFS should be regarded as active. Thus, the AFS is not only active in the Northern SSW–NNE-striking segment, where multiple evidences for recent tectonic activity are reported (Fig. 3, 4; Weissl et al. 2017), but also further to the South, where surface expressions of the fault are blanketed by Late Pleistocene and Holocene Danube sediments.

The level of confidence in the 1D geomechanical model is affected by a few issues. Due to uncertainty in the unlogged section, the S_v magnitude is potentially affected by an overestimation in the range of 5% to 9% at 750 m MD, that quickly becomes less relevant with depth, as at 2103.1 m MD the potential error is between 1.6% and 3%. The low confidence conversion from dynamic to static Poisson's ratio might result in an error of the estimated stress magnitudes in the range of ± 3.7 –4.2%. A few high-frequency spikes in the modeled stresses result from spikes in the calculated rock properties that could not be avoided using a smoothing filter. These small scale errors do not affect the geomechanical model significantly as the validation and general evaluation of the model are performed considering longer intervals rather than individual data in the spikes. The only problematic interval in the well

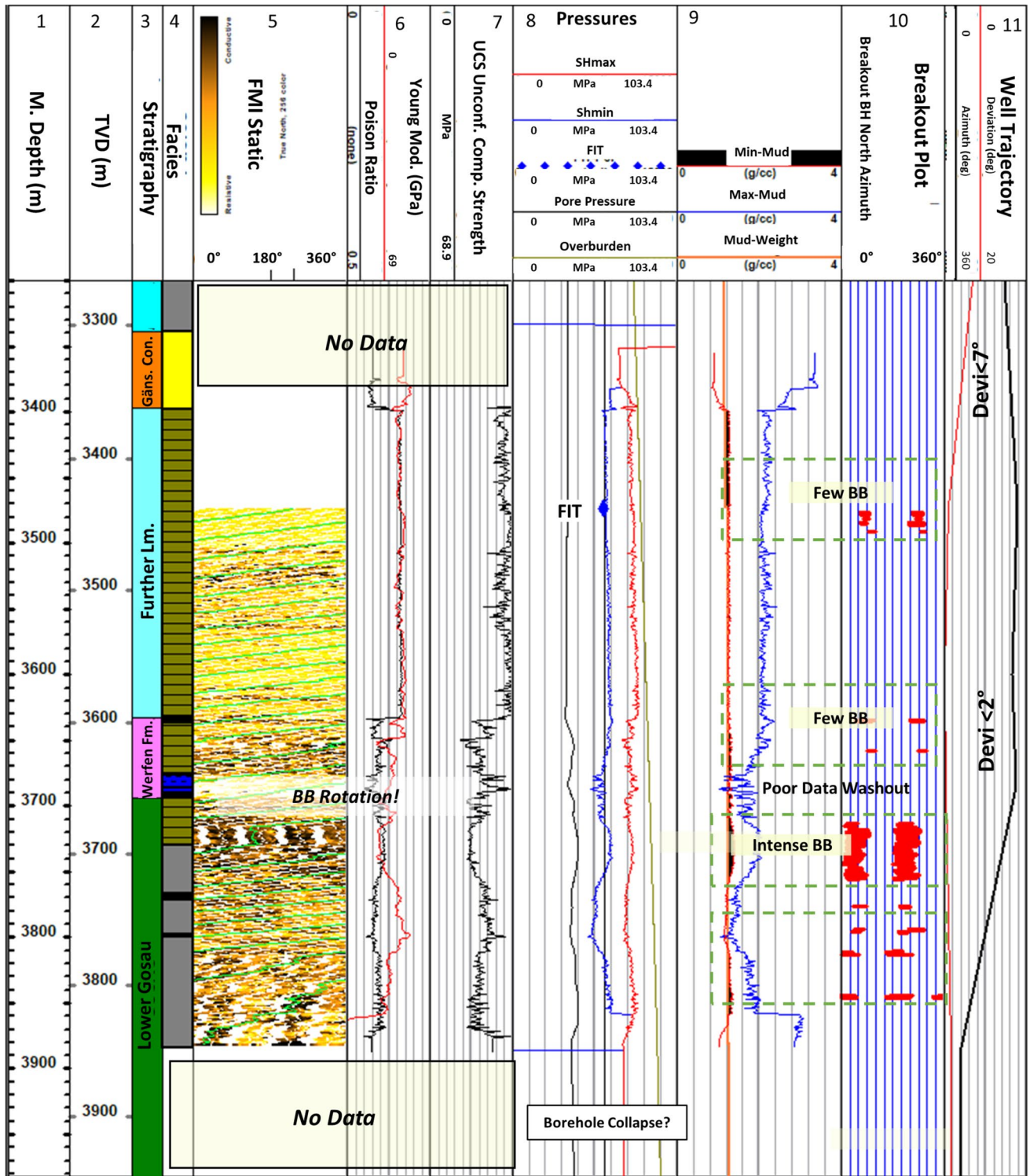


Fig. 15 1D geomechanical model of the lower part of Well 1 (3473–3888 m). Stress magnitudes are plotted in track 8 together with pore pressure and the formation integrity test (FIT). The stress model indicates normal faulting with $S_v > S_{Hmax} > S_{Hmin}$. Olive: S_v ; red: S_{Hmax} ; blue: S_{Hmin} ; black: pore pressure. Track 9 shows the well stability analysis with the Min-MUD curve (red) and Max-MUD curve (blue)

plotted against the actual mud density (Mud-Weight curve). Track 10 indicates the BO zones and the corresponding azimuth interpreted from the FMI. Green boxes indicate intervals where the model predicts BO, that partially correlate to potential BO detected by the FMI data

Fig. 16 Uninterpreted (A) and interpreted seismic section (B) across Well 1. Profile orientation is perpendicular to the strike of the ENE-dipping Seyring fault system (SFS) and the WSW-dipping Aderklaa fault system (AFS). Depth of fault intersections in (B) denote depth below sea level (1931 m = 2086 m TVD in Well 1; 2682 m = 2837 m TVD). See text for discussion

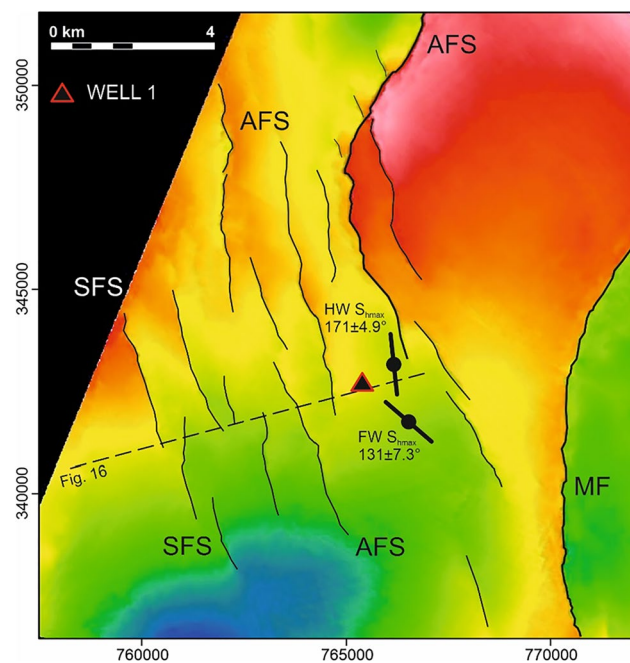
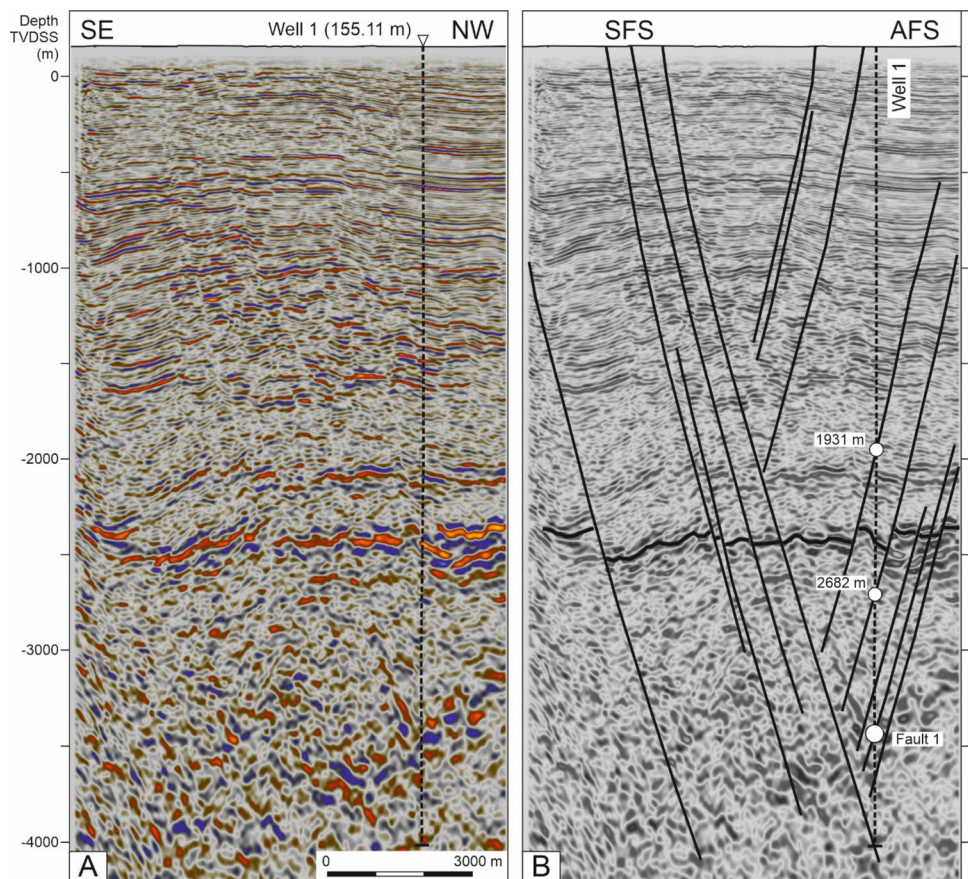


Fig. 17 Upper Sarmatian horizon map showing fault heaves of the Seyring (SFS) and Aderklaa fault system (AFS) and the location of Well 1. Bars denote the orientation of S_{Hmax} above (black) and below (gray) Fault 1 drilled at 3694 m depth (MD)

is a rather large washout in the lower part of the Werfen Fm. that resulted in a poor estimate of stress magnitudes (Fig. 15). The values in the poor quality interval were not used for any further geomechanical analysis. The estimation of the pore pressure is based only on the equilibrium during drilling and it not constrained by any actual measurements neither in Well 1, nor in nearby wells, as there are no published data in the Vienna Basin.

Model validation, in particular the estimation of S_{Hmax} by comparing modeled and actual stress-induced borehole failures, is not feasible in the depth intervals where the lack of appropriate log data prevents reliable detection of BO and DITF. In the interval with the two LOT the available calipers provide a reasonably reliable assessment of the occurrence of BO only in the 12.25 in section (2100–3179 m MD), in which there is rather good match between well stability analysis and potential BO. Well stability analysis indicates Mud-Weight < Min-MUD almost over the entire interval with several sections with big separation between the two curves, suggesting intense BO (Fig. 14). That partially agrees with the potential BO from caliper curves and indicates that the magnitude of S_{Hmax} cannot be much higher than the modeled one as this would result in excessive BO or even borehole collapse. Between 750 and 2090 m (17.75 in section) the model cannot be validated. However, S_{Hmax} is estimated with

similar gradient as in the 12.25 in section. In the lower part of the well (3473–3888 m MD), the lack of LOTs limits the reliability of the estimation of S_{hmin} , whereas the presence of FMI data allow for a validation of the model. In this section, a few intervals with borehole enlargements afflicted the sonic log and potentially also the density log, resulting in potential issues in the estimation of the elastic moduli and thus also the stress magnitudes. These intervals were not used to validate the model and do not affect the model in nearby intervals.

In spite of the discussed limitations, the 1D geomechanical model clearly indicates that the stress regime is a normal-faulting regime with $S_v > S_{\text{Hmax}} > S_{\text{hmin}}$. The stress regime appears particularly well constrained for the depth below about 1700 m where $S_v \gg S_{\text{Hmax}} > S_{\text{hmin}}$ (Figs. 14, 15). As the stress regime is normal faulting over the entire modeled interval, $S_1 = S_v$, $S_2 = S_{\text{Hmax}}$ and $S_3 = S_{\text{hmin}}$. As no other 1D geomechanical data have been published so far in the Vienna Basin, these observations cannot be compared to any other model.

In the Vienna Basin, all the available focal mechanisms indicate a strike-slip regime in the center of the basin, where the regional strike-slip fault system is located (Fig. 2), whereas there is no earthquake data to constrain the stress regime in the central part of the basin, close to the location of Well 1. Instead, there is unequivocal geological evidence for a normal faulting regime from faulted Late Pleistocene sediments recorded in several paleoseismological trenches located N-NE of Vienna (Fig. 2) (Hintersberger and Decker 2014; Weissl et al. 2017; Hintersberger et al. 2018; Oppenauer et al. 2022).

Stress polygons at 754 m and 2103.1 m (MD), where the two leak off tests were performed, indicate rather stable conditions for suitable oriented faults with coefficient of friction (μ) in the range 0.6–0.8 (Fig. 13). The estimated S_{Hmax} magnitudes fit within the limits derived for both coefficients of friction. Values indicate little/no BO at 754 m MD and BO formed at 2103.1 m MD. At 3473 m MD, the stress field is less constrained, due to the limits of the FIT. The modeled S_{hmin} magnitude is about 2.3 MPa > FIT, whereas the magnitude of S_{Hmax} (74.9 MPa) indicates a rather stable normal faulting regime (Fig. 13).

The 1D geomechanical model indicates that in the upper part of the well (0–2000 m), the deviatoric stress (in this case S_v – S_3 as the stress is normal faulting) is rather small, whereas below 2000 m it is increasing with a higher gradient (Fig. 18). Two faults of the AFS identified on the seismic data go through the path of Well 1 at depth 2086 m and 2837 m (TVD) in the interval not covered by the FMI data (Fig. 16). Two Mohr-diagrams were generated for the two faults, based on the corresponding geomechanical model, with fault orientation similar to the AFS and for two values of coefficient of friction (μ) 0.6 and 0.8, which are

reasonable values for regular faults (Fig. 18). Both faults of the AFS are far away from critical conditions for both values of the coefficient of friction. Calibrated Mohr-circles are far away from the failure envelopes, which suggests that the faults are probably not critically stressed, unless they are very weak ($\mu < 0.6$).

Below 3000 m, the onset of progressively overpressured fluids (below 3000 m) (Fig. 11) further shifts the system, already characterized by high deviatoric stress, towards critical conditions (Fig. 18). The Mohr diagram for Fault 1 (3694 m, 3657 m TVD) confirms that in the case of a weak fault ($\mu = 0.6$) the system is close to critical conditions (red line touching the envelope), whereas for a strong fault ($\mu = 0.8$) the system is in stable conditions (blue line not touching the envelope) (Fig. 18). Two stress polygons were computed for the conditions close to Fault 1, assuming two different values of the coefficient of friction μ for a weak fault (0.6) and strong fault (0.8) (Fig. 19). As shown also in Fig. 18, in case of a weak fault the system is already close to critical conditions, whereas in case of a strong fault the system is currently stable, but it could be destabilizing by an increase of pore pressure of 6.4 MPa (Fig. 19). These results agree with the observed stress rotation taking place at Fault 1, interpreted as resulting from active faulting.

Conclusions

The analysis of stress-induced borehole failures and 1D geomechanical modeling of the geothermal exploration Well 1 penetrating the Aderklaa Fault System (AFS) in the Vienna Basin proves that the drilled potential geothermal reservoirs are in a normal fault stress regime with $S_v > S_{\text{Hmax}} > S_{\text{hmin}}$, thus $S_1 = S_v$, $S_2 = S_{\text{Hmax}}$ and $S_3 = S_{\text{hmin}}$. BO evidence a rotation of S_{Hmax} from close to N-S in the hanging wall of a drilled branch fault of the AFS (Fault 1) to NNW-SSE, i.e., parallel to the strike of the fault. Stress rotation suggests that the drilled fault is active. This interpretation is in line with geological surface data from the northern continuation of the AFS that likewise proves Quaternary fault activity.

In spite of the partial incompleteness open hole, caliper and image logs, a 1D stress model could be calculated which appears sufficiently reliable to support decisions about the feasibility of deep geothermal heat production. While stress magnitudes in the upper part of the well (down to a depth of about 2000 m) are significantly below the magnitudes that would trigger the rupture of critically oriented faults including the AFS, stresses in the lower part of the drilled section in the pre-Neogene basement (below about 3300 m) are not. The geothermal development of reservoirs in the upper (“stable”) part of the drilled succession may, therefore, be practicable provided that it can be shown that the re-injection of cooled water

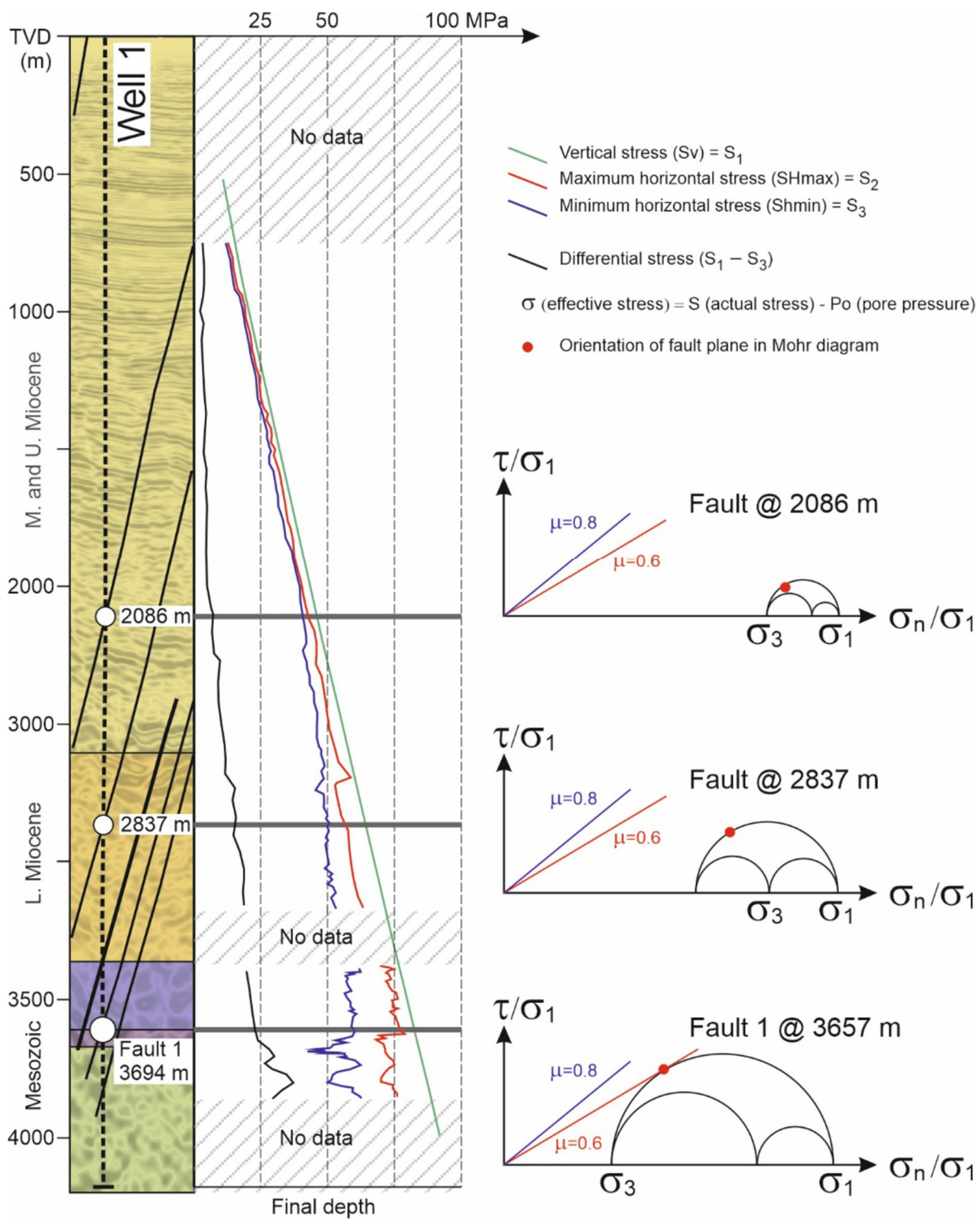


Fig. 18 Near-well section, stress magnitudes and differential stress calculated from the 1D-stress model of Well 1. Above the depth of about 2000 m TVD differential stress increases only slightly. Below 2000 m the increase of differential stress with depth is significantly higher. Excursions of the curves representing S_1 , S_2 and S_3 below about 3700 m TVD are partly due to poor borehole conditions that bias the sonic log data. Mohr circles illustrate effective stresses at

the depths of three faults of the AFS intersecting Well 1. Note that the distance to failure, indicated by the proximity of the Mohr circle to the failure envelopes, decreases with depth. Failure envelopes are shown for “strong” ($\mu=0.8$) and “weak” ($\mu=0.6$) faults. The Mohr circle for Fault 1 at 3657 m TVD (=3694 m MD) suggests that the fault is close to critical stressing

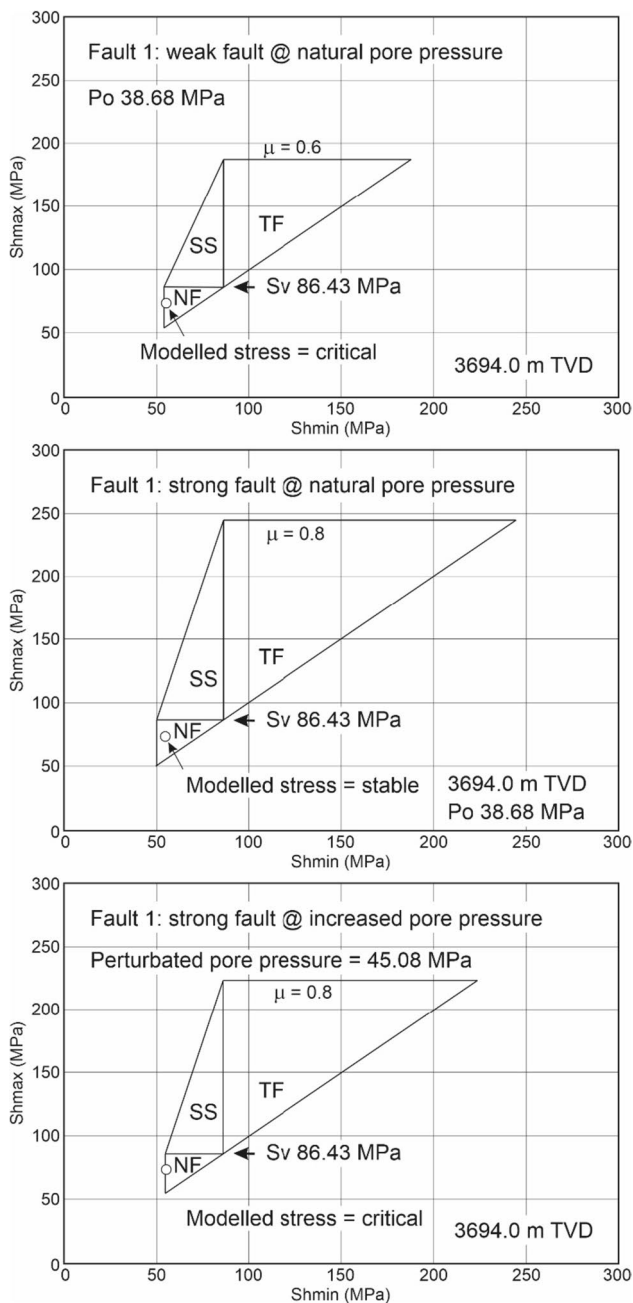


Fig. 19 Stress polygons of the estimated stress field in the vicinity of Fault 1 at 3657 m TVD (3694 m MD), which is associated to the stress rotation. Two polygons represent the present-day conditions with coefficient of friction (μ) 0.6 (weak fault) and 0.8 (strong fault). For the weak fault the conditions are close to critically stressed. For the strong fault, an increase of 6.4 MPa of the pore pressure is sufficient to destabilize the fault, as shown in the polygon in the lower part

would only lead to reductions of S_{hmin} that are still remote from instable conditions. In the deeper “instable” part of the succession data particularly highlights the drilled Fault 1 in 3694 m depth. The calculated stress polygon proves that stressing of the fault is close to critical. It has to be

assumed that the same is true for all other faults in the pre-Neogene basement that have similar orientations with respect to S_v . Near-critical stressing consequently is also likely for other branches of the AFS oriented sub-parallel to Fault 1 and faults belonging to the ENE-dipping Seyring Fault System (SFS), which are symmetrical with respect to S_v and the AFS. The safety case to exclude unintended triggering of seismic fault slip by developing geothermal reservoirs in close vicinity to one of the branch faults of the AFS and SFS may therefore be difficult or impossible to make.

As many of the faults in the studied part of the Vienna Basin are curved (Fig. 17), it is unclear how far a dynamic rupture would propagate along the fault. The stress data from Well 1 indicate that mostly the NNW–SSE-striking segments of the AFS system would be at risk of destabilization, whereas the potential reactivation also of the N–S-striking fault strands is difficult to assess. However, earthquake magnitudes of up to $M = 6.4$ derived from paleoseismological data from the SFS (Oppenauer et al. 2022) prove that the ruptured fault areas were sufficiently large to create earthquakes of such magnitudes. It is concluded that at least some dynamic ruptures were not confined to NNW–SSE-striking fault segments, because these are too small to create earthquakes with the observed magnitude.

We conclude that structural analyses of borehole image data and stress models built on open hole logs are important tools to evaluate the potential of unintended seismic fault triggering by geothermal heat production and the re-injection of cooled water. To utilize the full potential of the methods exploration wells should, from the beginning, be planned to collect all necessary tests and log data. Our case study identified the lack of a sufficient number of LOTs, incomplete log coverage of the drilled succession, and unavailability of image logs as the most important factors limiting the reliability the resulting model. Planning of exploration wells should therefore not limit the acquisition of such data to the targeted reservoir interval.

Acknowledgements The authors thank Wien Energie Gbmh and FFG for supporting research in the frame of the project GeoTief EXPLORE 3D (FFG Project No. 865009 of FFG’s e!MISSION program; University of Vienna Project No. FA 536 035). OMV provided access to 2D seismic data. We are in debt to Katerina Schöpfer for technical support and critical discussion of the stress results. We would also like to thank TerraSciences for providing an academic license of the TerraStation software. The authors wish to thank the editor M. Stipp, B. Müller and an anonymous reviewer for providing constructive comments that greatly improved the quality of the paper.

Funding Open access funding provided by University of Vienna.

Data availability The data that support the findings of this study are not openly available due to reasons of sensitivity and are available from the corresponding author upon reasonable request.

Declarations

Conflict of interest The authors declare that they have not conflict of interest.

Open Access This article is licensed under a Creative Commons Attribution 4.0 International License, which permits use, sharing, adaptation, distribution and reproduction in any medium or format, as long as you give appropriate credit to the original author(s) and the source, provide a link to the Creative Commons licence, and indicate if changes were made. The images or other third party material in this article are included in the article's Creative Commons licence, unless indicated otherwise in a credit line to the material. If material is not included in the article's Creative Commons licence and your intended use is not permitted by statutory regulation or exceeds the permitted use, you will need to obtain permission directly from the copyright holder. To view a copy of this licence, visit <http://creativecommons.org/licenses/by/4.0/>.

References

- ACORN (2004) Catalogue of earthquakes in the Region of the Alps—Western Carpathians—Bohemian Massif for the period from 1267 to 2004. Computer File, Vienna (Central Institute for Meteorology and Geodynamics, Department of Geophysics Brno (Institute of Physics of the Earth, University Brno)
- Alam J, Chatterjee R, Dasgupta S (2019) Estimation of pore pressure, tectonic strain and stress magnitudes in the Upper Assam basin: a tectonically active part of India. *Geophys J Int* 216:659–675
- Apoloner M-T, Tary J-B, Bokelmann G (2015) Ebreichsdorf 2013 earthquake series: relative location. *Austrian J Earth Sci* 108:199–208
- Arzmüller G, Buchta S, Rallbovský E, Wessely G (2006) The Vienna basin. In: Golonka J, Picha FJ (Eds) *The Carpathian and their foreland: geology and hydrocarbon resources*. AAPG Memoir 84, Tulsa, pp 191–204
- Aydin A, Nur A (1982) Evolution of pull-apart basins and their scale independence. *Tectonics* 11:91–105
- Baisch S, Weidler R, Vörös R, Wyborn D, de Graaf L (2006) Induced seismicity during the stimulation of geothermal HFR reservoir in the Cooper basin. *Bull Seism Soc Am* 96:2242–2256. <https://doi.org/10.1785/0120050255>
- Barton CA, Zoback MD (1994) Stress perturbations associated with active faults penetrated by boreholes: possible evidence for near-complete stress drop and new technique for stress magnitude measured. *J Geophys Res* 99:9373–9390. <https://doi.org/10.1029/93JB03359>
- Beidinger A, Decker K (2011) 3D geometry and kinematics of the Lasse flower structure: implications for segmentation and seismotectonics of the Vienna Basin strike-slip fault, Austria. *Tectonophysics* 499:22–40. <https://doi.org/10.1016/j.tecto.2010.11.006>
- Beidinger A, Decker K, Roch KH (2011) The Lasse segment of the Vienna Basin fault system as a potential source of the earthquake of Carnuntum in the fourth century A.D. *Int J Earth Sci* 100:1315–1329. <https://doi.org/10.1007/s00531-010-0546-x>
- Bell JS (1990) Investigating stress regimes in sedimentary basin using information from oil industry wireline logs and drilling records. In: Hurst A, Lovell M, Morton A (Eds) *Geological applications of wireline logs*. Geological Society Special Publication, vol 48, pp 305–325
- Blake OO, Faulkner DR, Tatham DJ (2019) The role of fractures, effective pressure and loading on the difference between the static and dynamic Poisson's ratio and Young's modulus of Westerly granite. *Int J Rock Mech Min Sci* 116:87–98. <https://doi.org/10.1016/j.ijrmms.2019.03.001>
- Blake OO, Ramscook R, Faulkner DR, Lyare UC (2020) the effect of effective pressure on the relationship between static and dynamic Young's Moduli and Poisson's ratio of Naparima Hill Formation Mudstones. *Rock Mech Rock Eng* 53:3761–3778. <https://doi.org/10.1007/s00603-020-02140-0>
- Brudy M, Zoback MD, Fuchs K, Rummel F, Baumgärtner J (1997) Estimation of the complete stress tensor to 8 km depth in the KTB scientific drill holes: Implications for crustal strength. *J Geophys Res* 102:18453–18475. <https://doi.org/10.1029/96JB02942>
- Buijze L, van Bijsterveldt L, Cremer H, Paap B, Veldkamp H, Wassing B, van Wees J, Yperen G, ter Heege J, Jaarsma B (2020) Review of induced seismicity in geothermal systems worldwide and implications for geothermal systems in the Netherlands. *Neth J Geosci* 98:e13. <https://doi.org/10.1017/njg.2019.6>
- Castagna JP, Batzle ML, Eastwood RL (1985) Relationships between compressional-wave and shear-wave velocities in clastic silicate rocks. *Geophysics* 50:571–581. <https://doi.org/10.1190/1.1441933>
- Castagna JP, Batzle ML, Kan TK, Backus MM (1993) Rock physics—the link between rock properties and AVO response. In: Castagna JP, Backus M (eds) *Offset-dependent reflectivity—theory and practice of AVO analysis*. SEG, Tulsa, pp 135–171
- Catali F, Men-Andrin M, Wiemer S (2013) The role of Coulomb stress changes for injection-induced seismicity: the Basel enhanced geothermal system. *Geophys Res Lett* 40:72–77. <https://doi.org/10.1029/2012GL054147>
- Chang C, Zoback MD, Khaksar A (2006) Empirical relations between rock strength and physical properties in sedimentary rocks. *J Pet Sci Eng* 51:223–237. <https://doi.org/10.1016/j.petrol.2006.01.003>
- Choi W, Park JW, Kim J (2019) Loss assessment of building and contents damage from the potential earthquake risk in Seoul, South Korea. *Nat Hazards Earth Syst Sci* 19:985–997
- Decker K (1996) Miocene tectonics at the Alpine-Carpathian junction and the evolution of the Vienna Basin. *Mitt Ges Geol Bergbaustud* 41:33–44
- Decker K, Peresson H, Hinsch R (2005) Active tectonics and Quaternary basin formation along the Vienna Basin Transform fault. *Quat Sci Rev* 24:305–320. <https://doi.org/10.1016/j.quascirev.2004.04.012>
- Decker K, Burmester G (2008) Stress orientations and active fault kinematics of the Vienna Basin Fault System, Austria. In: 3rd World Stress Map Conference, *Frontiers of Stress Research*, Helmholtz Centre Potsdam, GFZ German Research Centre for Geosciences, Abstracts, p 110
- Decker K, Peresson H (1996) Tertiary kinematics in the Alpine-Carpathian-Pannonian system: links between thrusting, transform faulting and crustal extension. In: Wessely G, Liebl W (eds) *Oil and gas in Alpidic thrustbelts and basins of Central and Eastern Europe*. EAGE spec pub 5, pp 69–77
- Deichmann N, Ernst J (2009) Earthquake focal mechanisms of the induced seismicity in 2006 and 2007 below Basel. *Swiss J Geosci* 102:457. <https://doi.org/10.1007/s00015-009-1336-y>
- Diehl T, Kraft T, Kissling E, Wiemer S (2017) The induced earthquake sequence related to the St. Gallen deep geothermal project (Switzerland): fault reactivation and fluid interactions imaged by microseismicity. *J Geophys Res Solid Earth* 122(9):7272–7290
- Eaton BA (1975) The equation for geopressure prediction from well logs. *Society of Petroleum Engineers*, paper SPE 5544. <https://doi.org/10.2118/5544-MS>
- Evans KF, Zappone A, Kraft T, Deichmann N, Moia F (2012) A survey of the induced seismic responses to fluid injection in geothermal and CO2 reservoirs in Europe. *Geothermics* 41:30–54
- Fuchs W, Grill R (1984) *Geologische Karte von Wien und Umgebung (1:200000)*. Geologische Bundesanstalt, Vienna

- Gangl G (1975) Seismotektonische Untersuchungen am Alpenostrand. Mitt Österreichischen Geol Ges 66–67:33–48
- Grigoli F, Cesca S, Rinaldi AP, Manconi A, López-Comino JA, Clinton JF, Westaway R, Cauzzi C, Dahm T, Wiemer S (2018) The November 2017 Mw 5.5 Pohang earthquake: a possible case of induced seismicity in South Korea. *Science* 360:1003–1006
- Gutdeutsch R, Aric K (1988) Seismicity and neotectonics of the East Alpine-Carpathian and Pannonian area. AAPG Mem 45:183–194
- Hammerl C, Lenhardt WA (2013) Erdbeben in Niederösterreich von 1000 bis 2009 n. Chr. *Abh Geol BA* 67:3–297
- Häring MO, Schanz U, Ladner F, Dyer BC (2008) Characterisation of the Basel 1 enhanced geothermal system. *Geothermics* 37:469–495
- Harzhauser M, Kranner M, Mandic O, Strauss P, Siedl W, Piller W (2020) Miocene lithostratigraphy of the northern and central Vienna Basin (Austria). *Austrian J Earth Sci* 113:169–200
- Heidbach O, Barth A, Müller B, Reinecker J, Stephansson O, Tingay M, Zang A (2016) WSM quality ranking scheme, database description and analysis guidelines for stress indicator. WSM Scientific Technical Report 16-01
- Hinsch R, Decker K, Wägreich M (2005) 3-D mapping of segmented active faults in the southern Vienna Basin. *Quat Sci Rev* 24:321–336. <https://doi.org/10.1016/j.quascirev.2004.04.011>
- Hintersberger E, Decker K, Lomax J, Lüthgens C (2018) Implications from palaeoseismological investigations at the Markgrafenriedl Fault (Vienna Basin, Austria) for seismic hazard assessment. *Nat Hazard* 18:531–553. <https://doi.org/10.5194/nhess-18-531-2018>
- Hintersberger E, Decker K (2014) A seismic gap at the central Vienna Basin Transfer Fault (Vienna Basin, Austria)? *Geophysical Research Abstracts Vol. 16*. EGU2014-14737
- Hölzel M, Decker K, Zámolyi A, Strauss P, Wägreich M (2010) Lower Miocene structural evolution of the central Vienna Basin (Austria). *Mar Pet Geol* 27:666–681. <https://doi.org/10.1016/j.marpetgeo.2009.10.005>
- Jarosinski M (1998) Contemporary stress field distortion in the Polish part of the Western Outer Carpathians and their basement. *Tectonophysics* 297:91–119. [https://doi.org/10.1016/S0040-1951\(98\)00165-6](https://doi.org/10.1016/S0040-1951(98)00165-6)
- Kim WY (2013) Induced seismicity associated with fluid injection into a deep well in Youngstown, Ohio. *J Geophys Res Solid Earth* 118:3506–3518. <https://doi.org/10.1002/jgrb.50247>
- Kirsch G (1898) Die Theorie der Elastizität und die Bedürfnisse der Festigkeitslehre. *Z Verlines Dtsch Ing* 42:707
- Kröll A, Wessely G (1993) Wiener Becken und angrenzende Gebiete: Strukturkarte-Basin der tertiären Beckenfüllung. Geologische Bundesanstalt, Vienna
- Kwiatek G, Martínez-Garzón P, Dresden G, Bohnhoff M, Hartline C (2015) Effects of long-term fluid injection on induced seismicity parameters and maximum magnitude in northwestern part of The Geysers geothermal field. *J Geophys Res Solid Earth* 120:7085–7101. <https://doi.org/10.1002/2015JB012362>
- Lal M (1999) Shale stability: drilling fluid interaction and shale strength. In: SPE Asian Pacific Oil and Gas Conference and Exhibition, 20–22 April, Jakarta, Indonesia. SPE 54356. <https://doi.org/10.2118/54356-MS>
- Lee EY, Wägreich M (2017) Polyphase tectonic subsidence evolution of the Vienna Basin inferred from quantitative subsidence analysis of the northern and central parts. *Int J Earth Sci* 106:687–705
- Leila M, Sen S, Abioui M, Moscariello A (2021) Investigation of pore pressure, in-situ stress state and borehole stability in the West and South Al-Khilala hydrocarbon fields, Nile Delta, Egypt. *Geomech Geophys Geo-Energy Geo-Resour* 7:56. <https://doi.org/10.1007/s40948-021-00256-3>
- Lenhardt WA, Švancara J, Melichar P, Pazdírková J, Havří J, Sýkorová Z (2007) Seismic activity of the Alpine-Carpathian-Bohemian Massif region with regard to geological and potential field data. *Geol Carpathica* 58:397–412
- Levi N, Habermueller M, Exner U, Wiesmayr G, Decker K (2021) Active out-of-sequence thrusting in the Molasse Basin constrained by a multidisciplinary approach (Eastern Alps, Austria). *Tectonophysics* 812:228911. <https://doi.org/10.1016/j.tecto.2021.228911>
- Majer EL, Baria R, Stark M, Oates S, Bommer J, Smith B, Asasuma H (2007) Induced seismicity associated with Enhanced Geothermal Systems. *Geothermics* 36:185–222. <https://doi.org/10.1016/j.geothermics.2007.03.003>
- Marsch F, Wessely G, Sackmaier W (1990) Borehole-breakouts as geological indications of crustal tensions in the Vienna Basin. In: Rossmannith HP (ed) *Mechanics of jointed and faulted rock*. CRC Press, Boca Raton, pp 113–116
- Martínez-Garzón P, Kwiatek G, Bohnhoff M, Dresden G (2016) Impact of fluid injection on fracture reactivation at The Geysers geothermal field. *J Geophys Res Solid Earth* 121:7432–7449
- Militzer HSP (1973) Einige Beiträge der Geophysik zur Primaerdatenerfassung im Bergbau. *Neu Bergbautechnik* 3:21–25
- Moos D, Zoback MD, Bailey L (1999) Feasibility study of the stability of open hole multilaterals, Cook Inlet, Alaska. SPE Mid-Continent Operation Symposium, Oklahoma City, Society of Petroleum Engineers
- Moos D, Zoback MD (1990) Utilization of observation of well bore failure to constrain the orientation and magnitude of crustal stresses: application to continental deep sea drilling project and oceanic drilling program boreholes. *J Geophys Res Solid Earth* 95:9305–9325. <https://doi.org/10.1029/JB095iB06p09305>
- Morawietz S, Heidbach O, Reiter K, Ziegler M, Rajabi M, Zimmermann G, Müller B, Tingay M (2020) An open-access stress magnitude database for Germany and adjacent regions. *Geotherm Energy* 8:1–39
- Moser M, Piros O (2018) Eine Revision des Begriffes “Further Kalk” bei Furth an der Triesting in den Gutensteiner Alpen (Niederösterreich). *Jahrb Geol Bundesanst* 158:59–64
- Najibi AR, Ghafoori M, Lashkaripour GR, Asef M (2017) Reservoir geomechanical modeling: In-situ stress, pore pressure, and mud design. *J Pet Sci Eng* 151:31–39. <https://doi.org/10.1016/j.petrol.2017.01.045>
- Nasir A, Hintersberger H, Decker K (2020) The 1906 Dobrá Voda earthquake (M=5.7) at the Vienna Basin Transfer Fault: evaluation of the ESI2007 intensity and analysis of the aftershock sequence. *Austrian J Earth Sci* 113:43–58. <https://doi.org/10.17738/ajes.2020.0003>
- Oppenauer L, Flores-Orozco A, Weissl M, Decker K (2022) Paleoseismology of the Seyring Fault in the Vienna Basin (Austria). PANGEO Austria 2022—Abstracts and Field Guides, 10–14 September 2022, Leoben. *Berichte Der Geologischen Bundesanstalt* 143:133
- Peresson H, Decker K (1997) Far-field effects of Late Miocene subduction in the Eastern Carpathians: E-W compression and inversion of structures in the Alpine-Carpathian-Pannonian region. *Tectonics* 16:38–56. <https://doi.org/10.1029/96TC02730>
- Pierdomenici S, Mariucci MT, Montone P (2011) A study to constrain the geometry of an active fault in southern Italy through borehole breakouts and downhole logs. *J Geodyn* 52:279–289. <https://doi.org/10.1016/j.jog.2011.02.006>
- Posch-Trötzlmüller G, Peresson M (2010). Geologische Bearbeitung kurzfristiger Aufschlüsse in Niederösterreich mit Schwerpunkt auf infrastrukturelle Bauten in schlecht aufgeschlossenen Regionen und auf rohstoffwissenschaftliche, umweltrelevante und grundlagenorientierte Auswertungen. Neue Bauaufschlüsse - Neues Geowissen: Niederösterreich. Geologische Bundesanstalt, Fachabteilung Rohstoffgeologie (unpublished), Vienna. Projekt NC 69/2009–2011, Jahresendbericht 2009

- Radwan A, Sen S (2021a) Stress path analysis for characterization of in situ stress state and effect of reservoir depletion on present-day stress magnitudes: reservoir geomechanical modeling in the Gulf of Suez Rift Basin, Egypt. *Nat Resour Res* 30:463–478. <https://doi.org/10.1007/s11053-020-09731-2>
- Radwan A, Sen S (2021b) Characterization of in-situ stresses and its implications for production and reservoir stability in the depleted El Morgan hydrocarbon field, Gulf of Suez rift basin, Egypt. *J Struct Geol* 148:10435510. <https://doi.org/10.1016/j.jsg.2021.104355>
- Reinecker J, Lenhardt WA (1999) Present-day stress field and deformation in Eastern Austria. *Int J Earth Sci* 88:532–550. <https://doi.org/10.1007/s005310050283>
- Royden, LH (1985) The Vienna Basin: a thin-skinned pullapart basin. In: Biddle KT, Christie-Blick N (eds) *SEPM Special Publications*, vol 37, pp 319–338
- SERIANEX (Trinational Seismic Risk Analysis Experts Group) (2009) Deep heat mining basel seismic risk analysis. Department für Wirtschaft, Soziales und Umwelt des Kantons Basel Stadt Amt für Umwelt und Energie
- Strauss P, Harzhauer M, Hinsch R, Wagreich M (2006) Sequence stratigraphy in a clastic pull-apart basin (Neogene, Vienna Basin). A 3D seismic based integrated approach. *Geol Carpath* 57:185–197
- Tóth L, Mónus P, Zsiros T (1999) Hungarian Earthquake Bulletin 1998. Geo-Risk, Budapest
- Wang Z (2000) Dynamic versus static elastic properties of reservoir rocks. *Seismic Acoust Velocities Reserv Rocks* 3:531–539
- Weissl M, Hintersberger E, Lomax J, Lüthgens C, Decker K (2017) Active tectonics and geomorphology of the Gaenserndorf Terrace in the Central Vienna Basin (Austria). *Quatern Int* 451:209–222. <https://doi.org/10.1016/j.quaint.2016.11.022>
- Wells DL, Coppersmith KJ (1994) New empirical relationship among magnitude rupture length, rupture width, rupture area, and surface displacement. *Bull Seismol Soc Am* 84:974–1002
- Wessely G (1988) Structure and development of the Vienna basin in Austria. In: Royden LH, Horváth F (eds) *American Association of Petroleum Geologists, Memoir*, vol 45, pp 333–346
- Witze A (2017) Risk of human-triggered earthquakes laid out in biggest-ever database. *Nature*. <https://doi.org/10.1038/nature.2017.22693>
- Woo J-U, Kim M, Sheen D-H, Kang T-S, Rhie J, Grigoli F, Ellsworth W, Giardini D (2019) An in-depth seismological analysis revealing a causal link between the 2017 M W 5.5 Pohang earthquake and EGS project. *J Geophys Res Solid Earth*. <https://doi.org/10.1029/2019JB018368>
- Yang J, Fu LY, Zhang Y, Han T (2022) Temperature-and pressure-dependent pore microstructures using static and dynamic moduli and their correlation. *Rock Mech Rock Eng* 55:4073–4092. <https://doi.org/10.1007/s00603-022-02829-4>
- Zoback MD (2007) *Reservoir geomechanics*. Cambridge University Press, Cambridge
- Zoback MD, Moos D, Mastin L, Anderson RN (1985) Well bore breakouts and in situ stress. *J Geophys Res* 90:5523–5530
- Zoback MD, Barton CA, Brudy M, Castillo DA, Finkbeiner T, Grolimund BR, Moos DB, Peska P, Ward CD, Wiprut DJ (2003) Determination of stress orientation and magnitude in deep wells. *Int J Rock Mech Min Sci* 40:1049–1076. <https://doi.org/10.1016/j.ijrmms.2003.07.001>